

Mid-infrared size survey of Young Stellar Objects: Description of Keck segment-tilting experiment and basic results

J. D. Monnier¹, P. G. Tuthill², M. Ireland², R. Cohen³, A. Tannirkulam¹, and M. D. Perrin⁴

ABSTRACT

The mid-infrared properties of pre-planetary disks are sensitive to the temperature and flaring profiles of disks for the regions where planet formation is expected to occur. In order to constrain theories of planet formation, we have carried out a mid-infrared ($\lambda = 10.7\mu\text{m}$) size survey of young stellar objects using the segmented Keck telescope in a novel configuration. We introduced a customized pattern of tilts to individual mirror segments to allow efficient sparse-aperture interferometry, allowing full aperture synthesis imaging with higher calibration precision than traditional imaging. In contrast to previous surveys on smaller telescopes and with poorer calibration precision, we find most objects in our sample are partially resolved. Here we present the main observational results of our survey of 5 embedded massive protostars, 25 Herbig Ae/Be stars, 3 T Tauri stars, 1 FU Ori system, and 5 emission-line objects of uncertain classification. The observed mid-infrared sizes do not obey the size – luminosity relation found at near-infrared wavelengths and a companion paper will provide further modelling analysis of this sample. In addition, we report imaging results for a few of the most resolved objects, including complex emission around embedded massive protostars, the photoevaporating circumbinary disk around MWC 361A, and the subarcsecond binaries T Tau, FU Ori and MWC 1080.

Subject headings: accretion disks — radiative transfer — instrumentation: interferometers — circumstellar matter — stars: pre-main sequence — stars: formation

1. Introduction

Theories of planet formation rely on observational estimates of preplanetary disk initial conditions in order to make predictions. By connecting detailed and accurate disk initial conditions with the observed diversity of exoplanetary systems, these theories promise to explain how, when

¹University of Michigan, Department of Astronomy

²University of Sydney

³W. M. Keck Observatory

⁴University of California at Los Angeles

and where exoplanets form under a wide range of circumstances. Unfortunately, direct measurements of the initial conditions are very uncertain since these regions remain largely unresolved by conventional observing techniques. Indeed, disk theory is still undergoing active revision and new measurements more often reveal puzzling surprises rather than build confidence in pre-existing models.

Pioneering near-infrared observations of young stellar objects (YSOs) using long-baseline interferometry (Millan-Gabet et al. 1999, 2001; Tuthill et al. 2001) found disk emission sizes that were much larger than expected from the conventional disk theory. This has been successfully interpreted in terms of an optically-thin cavity surrounding the star, in contrast to previous assumptions of an optically-thick disk extending to stellar surface (Monnier & Millan-Gabet 2002; Natta et al. 2001; Monnier et al. 2005). While most work has been done for the intermediate mass Herbig Ae/Be stars, this general pattern is seen even for the young sun analogues, the T Tauri stars (Akeson et al. 2005; Eisner et al. 2005; Millan-Gabet et al. 2007).

The introduction of this large inner cavity to explain the near-infrared sizes radically changed the inner disk structure in models of these systems, requiring a “puffed-up inner rim” and even a shadowed region behind the rim in some models (Dullemond et al. 2001). In order to probe the disk structure and surface temperatures at these larger radii, we need to observe at longer wavelengths. Mid-infrared size measurements using interferometric techniques promise to probe the terrestrial-planet forming zones around young stars, characterized by temperatures around 300K. Until recently, most attempts to resolve YSO targets in the mid-IR have failed due to lack of angular resolution (e.g., Liu et al. 1996).

Hinz and collaborators have resolved a few targets using a novel nulling interferometer BLINC on a single 6.5m-aperture telescope (Hinz et al. 2001; Liu et al. 2005, 2007), although most targets were unresolved. Clearly, longer baselines will be needed to increase the angular resolution; the ISI interferometer was the first long-baseline interferometer to resolve thermal emission from a YSO (Lkh α 101; Tuthill et al. 2002).

A radical technological advance was recently made by the MIDI instrument on the VLTI interferometer, measuring seven mid-infrared sizes of Herbig Ae/Be stars (Leinert et al. 2004) and even taking a spatially-resolved spectra across the silicate feature (van Boekel et al. 2004). With baselines ranging from 10m to 200m, the VLTI-MIDI system (and also the Keck Interferometer Nuller; Stark et al. 2009) is poised to revolutionize studies of YSO disks in the mid-infrared.

In this article, we describe an experiment employing one of the world’s largest single-aperture telescope, the Keck-1 telescope. We have optimized the calibration precision of our survey by programming the individual mirror segments of the Keck to create multiple non-redundant interferometric arrays. In this method, we allow precise calibration of changing atmospheric conditions while instantaneously sampling full 2-dimensional sky angles, allowing detection of disk elongations and asymmetries with unprecedented precision. Furthermore, we can also survey sources very quickly, allowing a large sample to be observed in only a few nights. Our study complements longer-baseline

observations since “short” baselines are needed to distinguish between large-scale disk emission and emission from the compact “puffed-up inner rim” (van Boekel et al. 2005; Tannirkulam et al. 2007).

Here we report the full results of our diffraction-limited size survey of bright young stellar objects, finding most of them to be resolved and a few to be elongated. In addition to our imaging results, we can investigate the mid-infrared size – luminosity relations for YSOs in detail for the first time. Unfortunately, the recent decommissioning of the only mid-infrared camera on the Keck telescope marks the end of this short-lived but exciting experiment.

2. Observations

2.1. Description of segment-tilting experiment

While mid-infrared imaging with 10-m class telescopes is often considered “diffraction-limited,” precise measurements of partially-resolved objects are difficult due to changes in seeing between observing a target object and a Point Spread Function (PSF) calibrator. In order to circumvent these difficulties, we designed a novel interferometer experiment whereby individual segments of the 36-segment Keck telescope were reconfigured to form four interferometric arrays. Since each segment (1.8m across) is much smaller than the typical coherence length of the atmosphere ($r_0 = 5\text{--}10\text{m}$ at $\lambda = 10\mu\text{m}$) the results are more robust to variations in seeing conditions. The general approach of apodizing a telescope for interferometry is known as “aperture masking” and the technique has well-established advantages over speckle interferometry and adaptive optics for bright targets. We refer the interested reader to the pioneering work of Haniff et al. (1987) and the more recent implementation on Keck for further discussion (Tuthill et al. 2000).

In this work, we formed five interferometric sub-arrays by tilting the Keck primary mirror segments in a customized pattern. Figure 1a shows the Keck segment map color-coded by the applied tilt in a pattern known as “pattern 6” (while other tilt patterns were available, only pattern 6 was used in this work). These tilts caused the stellar image to split into 5 separate images as illustrated in Figure 1b. Four of the images (each with light from 6 segments) were arranged in a $5'' \times 5''$ square which fit perfectly on the $10'' \times 10''$ field-of-view of the Long Wavelength Spectrometer (LWS) camera on Keck-1, a 128×128 array with $0.83''$ platescale (Campbell & Jones 2004; Perrin 2006). The four images were used for science and were measured during data acquisition. The segments contributing to each of the four “science” arrays were arranged in a non-redundant pattern so that the fringe visibilities of all baseline pairs could be extracted using Fourier analysis (see discussion of redundancy in aperture masking interferometry in Tuthill et al. 2000). Because not all segments could be incorporated into four non-redundant patterns, a fifth image was created using light from the 12 unused segments and this light was projected $15''$ away from the detector.

This approach to aperture masking has a few significant advantages over those employing opaque masks placed in the telescope pupil plane (as done for all previous aperture masking work).

Firstly, since light from 24 of the 36 segments are used for science, the collecting area of the Keck primary is efficiently used (compare to near-infrared Keck aperture masking which passes 1-10% of the incident flux). Secondly, each of the four sub-arrays generally has different (u,v) Fourier coverage, which is essential for high fidelity aperture synthesis imaging. Indeed, we have already presented high-resolution images of dusty evolved stars (Weiner et al. 2006; Ireland et al. 2007), Wolf-Rayet stars (Rajagopal et al. 2007), and one YSO (Monnier et al. 2008) with unprecedented angular resolution. Thirdly, tilting segments is operationally straightforward and does not require any hardware modifications – we expect this technique to find application for the next generation of segmented telescopes, e.g., Gran Telescopio Canarias, Cornell Caltech Atacama Telescope, and the Thirty Meter Telescope.

2.2. Segment-tilting procedure

The segments were tilted by sending offsets to the 108 actuators which support and control the Keck primary mirror. For all segments in a subarray, offsets were calculated so that incoming light was reflected to the desired off-axis location in the telescope image plane. Note that in addition to the tilts, a large piston offset was needed to be applied to the segments in order to preserve phase coherence at each of the four new pointing origins. In essence, this extra piston term was necessary so that each subset of segments conformed to a new parabolic surface. These piston offsets can amount to $\sim 100\mu\text{m}$, critical to correct so that interferometric fringes fall within the coherence envelope of the light (typical narrow-band filters have $\frac{\lambda}{\Delta\lambda} \sim 7$).

In normal Keck operation, offsets between mirror segments are continuously monitored and maintained by the Keck Active Control System (ACS), employing capacitive edge sensors. However, our experiment required the edge sensors to operate with a lower gain setting due to the much larger gaps between segment edges encountered here. Unfortunately, the sensor response was not well-calibrated under these conditions, and so the actual tilts and pistons realized in practice only approximate the desired configuration (typical errors were $5''$). Fortunately, the introduced errors were found to be mostly corrected by employing so-called “focus mode” to the primary. “Focus mode” approximates telescope focus by changing the overall curvature of the Keck primary mirror surface. It is a well-known characteristic of the Keck ACS system that changing sensor gain settings introduce focus-mode error (Richard Cohen, private communication).

After correcting focus-mode errors, there were still residual tilt mismatches that affected some segments greatly. Clearly, if the light patterns from individual segment do not overlap well, the fringe power will be reduced and become sensitive to small changes of mirror figure (say, as a function of elevation). In order to optimize beam overlap, we applied a final correction using “optical feedback.” That is, we took a set of data at the beginning of each night using our best focus-mode alignment and analyzed the resulting fringe patterns to estimate correction terms for each segment. The algorithm we used employed phase slopes in the Fourier transform of the speckle patterns and would not have worked in the case of a redundant array of segments. We then applied

these small corrections as a perturbation to the existing ACS offsets. This entire procedure took approximately 10 minutes and resulted in excellent alignment, with individual segments overlapping with $\sim \frac{1}{10}''$ precision, approximately $0.1 \frac{\lambda}{D_{\text{segment}}}$. See Figure 2 showing short-exposure fringe images before and after the final “optical tweaking.”

It was found that the segment alignment could change by up to $\sim 0.5''$ as a function of telescope elevation and other operational variables (e.g., temperature), necessitating re-calibration. In general, we solved this by having separate actuator calibration “snapshots” as a function of elevation and using calibrator stars near to each target in time and elevation angle. For bright objects one can use post-processing to measure the tilts of each segment after the fact (akin to the “optical tweak” algorithm discussed above) and apply correction factors. We did not use this extra calibration step in this paper since the correction is signal-to-noise dependent and many of the YSOs were too faint for robust implementation.

2.3. Data collection methodology

We employed standard chop-nod observing methods to minimize noise from fluctuating background. The secondary mirror was chopped at 5 Hz with a $10''$ throw along the telescope azimuth direction. In general, each saved data frame had a total integration time of 90 ms and we collected approximately 350 individual chop-nod sets. We sometimes employed longer integrations and slower (2.5 Hz) chop cycles for faint targets, and also collected more chop-nod sets to improve signal-to-noise ratio. The 90 ms integration times were sufficient to essentially “freeze” any fringe blurring due to atmospheric turbulence at these wavelengths, although telescope wind-shake can still cause calibration problems; fortunately, wind-shake was minimal during the observations presented here. Each target was observed two independent times, bracketed by observations of point-source calibrators located nearby in the sky. Table 1 contains the complete observing log, including the target names, dates, times, and calibrators used. We observed all of our targets in only one filter, the $10.7\mu\text{m}$ filter (passband $9.92\text{--}11.47\mu\text{m}$).

2.4. Data reduction

The bulk of the data analysis processing was carried out by the same aperture masking code developed for the near-infrared version of the Keck masking experiment, which is best described in Monnier et al. (1999a) and Tuthill et al. (2000). The only major modification to the data pipeline was a change meant to address significant camera noise in the power spectra of our short exposure images. Here we used the nod sequences (which did not have any star light) to estimate a contemporaneous bias power spectrum. This bias subtraction proved necessary and key to extracting reliable results for the faintest targets in our sample.

The overall observing procedure was introduced in the first segment-tilting publications (Weiner et al.

2006; Rajagopal et al. 2007; Monnier et al. 2008). Essentially, each subarray pattern (field-of-view $3''$) was analyzed using Fourier techniques, resulting in fringe visibilities for each baseline and closure phases for all triangles. These values were calibrated using point-source reference stars. Some objects are very resolved and the shortest inter-segment spacing is approximately 2 meters long, meaning we are missing a lot of short-baselines. In order to make up for this, we also analyzed the same data frames using baselines shorter than 1.8 meters, which correspond to sampling the many redundant baselines within a segment. These short baselines are useful when reconstructing a wide binary companion during apertures synthesis imaging and helps to constrain information on the percentage of the light coming from a large-scale “halo” for some targets.

The measurements from the four simultaneous (inter-segment) patterns and the results of the “short-baseline” (intra-segment) measurements are merged together and used in subsequent analysis. We used observations of the known binaries MWC 1080 and SVS 20 to validate our position angles and plate scale. The calibrated data are saved in the OI-FITS data format for optical interferometry (Pauls et al. 2005) and are available upon request.

2.5. Analysis of Systematic Errors

Since we expected some of our target sample to be “unresolved” it was critical to establish reliable upper limits in those cases. This required an extensive analysis of systematic errors, as was recently done for near-infrared aperture masking data (Monnier et al. 2007).

The best method for reliable error estimation is to obtain multiple *independent* datasets for each object. This requirement was a driving consideration in our observing strategy and we obtained multiple observations for all our targets as can be seen in Table 1. By analyzing the consistency between the multiple independent measurements we can provide robust error analysis.

Figure 3 Shows a consistency plot for all the data of the Keck segment tilting experiment using Pattern 6 – this includes many objects not part of this YSO survey but still useful for the analysis of systematic errors. Here we graph the size measured for an object at one time against the size measured for the same target at another time (and nearly always using an independent calibrator sequence). To create this graph we removed known binaries (MWC 1080, T Tau, FU Ori) and the error bars were estimated by analyzing the 4-subarrays of pattern 6 using bootstrap sampling techniques. Based on the variation in measured diameter as function of mean diameter, we can quantitatively estimate our 2-sigma detection limit as FWHM 35 milliarcseconds – our confidence limits as a function of mean diameter are also included in Figure 3.

As was found in Monnier et al. (2007), the calibration precision is non-linear in the sense that the fractional error is very large for small sizes while being greatly reduced for larger sizes. Our final fitting results (both 1-D and 2-D) used bootstrap sampling of the different epochs and sub-arrays to capture calibration and systematic errors. In the case that two independent measurements disagreed dramatically, we removed this target from our sample. As can be seen in Figure 3, this

rarely occurred and did not significantly impact our sample size.

2.6. Aperture synthesis imaging

Aperture synthesis imaging can be carried out for the most resolved targets, useful for detecting faint diffuse emission and for detecting binary companions. We used the publicly available BSMEM image reconstruction software (Buscher 1994; Lawson et al. 2004, 2006) for aperture synthesis imaging. This program was discussed recently in Monnier et al. (2008) and was validated in more detail against the MACIM (Ireland et al. 2006) algorithm in Zhao et al. (2008). BSMEM uses the maximum entropy method (Gull & Skilling 1983; Narayan & Nityananda 1986) and is similar to the VLBMEM program (Sivia 1987) extensively used in the near-IR Keck masking project (e.g., Monnier et al. 1999b; Tuthill et al. 1999, 2000). While most young stellar objects were only partially resolved here, a few sources were large enough (on the sky) to be imaged and these are discussed in §3.3.

3. Results

Table 2 contains the complete source list for this work, including 5 embedded massive protostars, 25 Herbig Ae/Be stars, 3 T Tauri stars, 1 FU Ori systems, and 5 emission-line objects of uncertain classification. We have also included other important characteristics of our sample, including V, J, H, and K magnitudes, our measured $10.7\mu\text{m}$ flux within aperture of $3''$ diameter, the IRAS 12 and $25\mu\text{m}$ flux, and notation regarding the presence of a close binary companion (based on the literature). Subsequent tables and figures maintain the groupings and target orderings as presented in Table 2.

3.1. Visibilities

Figure 4 shows the squared-visibility data for all our targets as a function of baseline in meters. In this figure, we have performed (u,v) averaging on scales of 0.45 meters. This averaging is done in the (u,v) plane so baselines are only merged when sharing similar lengths and position angles. Here we did not average together results from the different independent observations, but rather overplotted each separate epoch detailed in Table 1. Thus, the observed scatter represents the combination of observing errors plus any position-angle dependency of the source structure. For instance consider the visibilities of v892 Tau and MWC 349A which vary for the same baseline length outside the error bars – indeed, these two objects are extremely asymmetric. Also consider that MWC 1080 and T Tau are both well-known sub-arcsecond binary stars – this is obvious in the scattered visibility data.

Figure 5 shows the squared-visibility as a 2-dimensional function of (u,v) coordinates, a useful presentation format for detecting elongations. For instance, the extreme asymmetry for MWC 349A and v892 Tau, inferred from the 1-D visibility curves, is quite evident here. Also, the large “halo” structure around MWC 361A, indicated by the sharp drop of visibilities as short baselines and then a plateau, can be easily spotted. The binary signatures in T Tau, FU Ori, and MWC 1080 are evident too, although it is difficult to interpret since the sinusoidal patterns are under-sampled, requiring analysis through imaging or model-fitting to extract the binary component separation.

3.2. Fitting Results

We have characterized the emission sizes of all targets by fitting the visibility data with both a circularly-symmetric (1-D) Gaussian model and an elliptical (2-D) Gaussian model. In both cases, we also allowed for a large-scale “halo” component, similar to the model used for near-infrared fitting of YSO visibilities in Monnier et al. (2006) which was motivated by earlier work (e.g. Leinert et al. 2001).

Table 3 contains the complete fitting results from our work. Error bars were estimated through bootstrap sampling of the multi-epoch data as well as from the different sub-arrays of “Pattern 6.” For each fit (1-D and 2-D) we also report the best fit χ^2_ν normalized by degrees of freedom. Thus, if the χ^2_ν value is greater than ~ 1 then we expect this model to be an incomplete description of the data. For instance for MWC 349A, the χ^2_ν is 4.0 for the circular-symmetric fit but decreases to 1.1 for a 2-dimensional Gaussian – we already discussed above that this object was clearly asymmetric. In most cases when the χ^2_ν is $\lesssim 1$ for the 1-D fit, then the 2-D fit is only marginally better and that there is no statistically-significant ellipticity detected. Some targets have high χ^2_ν even for the 2-dimensional Gaussian model, indicating a more complicated object. This is true for all the embedded YSOs which are generally the most resolved – these objects are ideal targets for aperture synthesis imaging in the next section §3.3.

3.3. Imaging

While most of the analysis in this work and the companion paper relies on the size-fitting results, we also report imaging results for the most resolved targets. We used the BSMEM image reconstruction program (see §2.6) on all targets and inspected the results. In Figure 6, we collected the images of all the objects that showed structures beyond a simple, partially-resolved Gaussian profiles and/or were larger than 70 mas in size. Note there are residual imaging artifacts at the level of a few percent of the peak, especially evident for the binary sources MWC 1080, T Tau and FU Ori. Notes on individual objects follow.

AFGL 490 has extension to south.

Mon R2 IRS 3 shows nebulosity along a N-NE to S-SW axis and a companion at $\rho = 836$ mas, $\theta = 16.7^\circ$, similar position to the companion first reported by McCarthy (1982) of separation 870 mas at PA 13.5° .

AFGL 2136 has a slight extension to west-southwest that appears in two independent sets.

AFGL 2591 emission has slight extension to west.

S140 IRS1 shows significant nebulosity to the South.

AB Aur is a prototypical Herbig Ae star which has been claimed to be elongated nearly 2-to-1 along PA 30° by Liu et al. (2005). We rule out this large level of elongation (supported by 4 separate observations over 3 different observing nights), although we do find a slight extension along this position angle in our image. Overall the emission is circularly symmetric, consistent with a nearly face-on geometry and in agreement with the conclusions of Mariñas et al. (2006).

v892 Tau was resolved into a circumbinary disk and was discussed in Monnier et al. (2008). Here, we reproduce the image.

LkH α 101 shows a slight elongation along North-South direction, similar to reported asymmetry in the near-infrared (Tuthill et al. 2002). Note we do not have fine enough angular resolution to resolve the dust-free cavity in the center reported by these authors.

R Mon is resolved approximately as much as AB Aur, showing mostly symmetrical emission.

Z CMa is a well-known close binary (~ 100 mas) recently imaged by Millan-Gabet & Monnier (2002). Here, the mid-infrared emission appears extended towards position angle $\sim 128^\circ$, which is the direction of the FU-Ori type companion. This extension could represent emission from a circumbinary disk or direct IR emission for the FU Orionis component to this system. Most likely, the bulk of the mid-IR emission is from the Herbig Be component of the system and not the FU Ori object.

MWC 349A is very elongated and the imaging shows a symmetric structure oriented along PA 95° , very similar to the PA 100° reported in the NIR (Danchi et al. 2001).

MWC 361A was found to have a large “halo” containing 45% of the flux at $10.7\mu\text{m}$. This halo was over-resolved on our shortest baselines. Our shortest baseline data suggested the halo was elongated north-south on arcsecond scales and this is confirmed by independent (standard full-aperture) LWS images taken at $11.6\mu\text{m}$ (SiC filter) and $17.65\mu\text{m}$. These images are shown in Figure 7; a full description of these observations and the data reduction appears in Perrin (2006). Note the N-S elongation of the extended emission matches the orientation of the binary orbit of MWC 361A measured by Monnier et al. (2006), strongly suggesting this halo is the remnant of a circumbinary disk. It is remarkable that the mid-IR disk emission is $>20\times$ bigger than the semi-major axis of the binary, indicating a huge disk gap in this system much larger than can be produced by disk clearing through dynamical interactions with the inner binary. Given the early spectral type of the primary star in this system, we suggest that photoevaporation of the circumbinary disk

is well underway.

MWC 1080 is binary with $\rho = 764$ mas, $\theta = -91.1^\circ$, comparable to the result of Leinert et al. (1997) of $\rho = 760$ mas, $\theta = -93^\circ$.

The T Tau companion to the south (which is itself a close binary) is detected at $\rho = 639$ mas, $\theta = -170.9^\circ$. We attempted a more sophisticated analysis to look for evidence of the tertiary to this system. Indeed, we find that the visibility and closure phase data can not be fit with a simple binary star (Skemer et al. 2008). However, there are calibration issues regarding field-of-view limitations caused by bandwidth-smearing that we have not corrected here. This issue will be tackled in a future paper.

We detect a companion to FU Ori at separation 488 mas and PA of 163.3° E of N, confirming the report by Wang et al. (2004) of a potential companion at separation 500 mas at PA 161° . As for T Tau, we can not report a reliable flux ratio due to unresolved issues with bandwidth smearing effects that have not yet been corrected.

3.4. Comparison to Literature

Our results are generally in agreement with results from the BLINC experiment by Hinz and collaborators (Hinz et al. 2001; Liu et al. 2005, 2007, excepting the elongation of AB Aur), although we note most of these workers’ measurements were upper-limits. We also compared our results to the long-baseline interferometry VLTI data of Leinert et al. (2004) and others (Quanz et al. 2006), finding that the Gaussian fits do not always agree between the two methods (our sizes typically larger). The size discrepancies can be understood if the long-baseline VLTI measurements are more sensitive to the properties of the hot inner wall while the short-baseline (single) Keck data can only probe the large-scale, outer flared disk (see discussion in van Boekel et al. 2005; Tannirkulam et al. 2007; Millan-Gabet et al. 2007). These observed differences appear to confirm the expectations from models that mid-infrared emission comes from (at least) two distinct spatial scales and we will need measurement from a wide range of scales in order to reconstruct the actual disk temperature profile.

4. Analysis

4.1. Size – Luminosity Diagram

A very tight correlation has been found between the near-infrared size of a young stellar object disk and the luminosity of the host star for Herbig Ae and late Be stars (Monnier & Millan-Gabet 2002; Monnier et al. 2005; Millan-Gabet et al. 2007). This simple correlation arises because the NIR emission only comes from the hottest dust near the evaporation front and the location of the

evaporation front is primarily sensitive to a single observable, the central luminosity.

The mid-infrared emission from young stars is expected to come from up to three regions: the hot inner wall located at the dust evaporation radius, a thin surface layer on the disk (e.g. van Boekel et al. 2005; Tannirkulam et al. 2008), and perhaps a circumstellar envelope (“halo”). Thus, the mid-infrared size and flux density will depend on multiple factors in addition to the central luminosity, depending most sensitively on the dust size distributions both vertically (setting temperature) and radially (controlling disk flaring). While it is beyond the scope of this paper to investigate these effects, we will discuss them generally in the context of the mid-IR size – luminosity diagram.

Figure 8 shows the mid-infrared size – luminosity diagram for the stars in our sample, constructed using the same procedure as in Monnier & Millan-Gabet (2002). Our sample represents a factor of 3 times increase in sample size over previous work and spans a large range of YSO luminosity. We used distances and luminosities from Acke & van den Ancker (2004) when available. In this diagram, we find a crude correlation of size with luminosity showing disk emission with characteristic temperatures of 250–900 K spanning about 5 orders of magnitude in luminosity. While the previously-published *near-infrared* size – luminosity diagram shows only about a factor of 2 scatter at a given luminosity, this mid-infrared relation shows much larger scatter, a factor of 5 or more. The origin(s) of the increased scatter and the breakdown in the size-luminosity relation will be the subject of a companion paper (Tannirkulam et al., in preparation). Here, we will only make general comments.

In Tannirkulam et al. (2008), the large mid-infrared size difference between two “twin” Herbig Ae stars (AB Aur and MWC 275) was explained through the influence of small grains in the AB Aur disk at radii of ~ 7 AU. These grains absorb stellar radiation effectively, heating up the disk and causing flaring. The origin of these small grains could be due to collisions between planetesimals or the release of small grains as ice-cemented dust agglomerates break apart at about ~ 10 AU. This example illustrates how variations between targets in the *radial* dust size distributions can explain some of the scatter in this diagram. Other modifications to the dust distribution, such as dust growth and settling, can also cause significant changes in mid-infrared SED (Dullemond & Dominik 2004; D’Alessio et al. 2006).

Another source of scatter is the presence of binaries. We have indicated close binaries in Table 2 and in Figure 8. For instance, the emission from v892 Tau was recently imaged to be from a circumbinary disk (Monnier et al. 2008) and we see in Figure 8 that v892 Tau is indeed oversized for its luminosity.

We also note that the embedded YSOs all cluster near the top-right of the diagram at high luminosities and low temperatures. This is expected since the high optical depths toward these Class I objects mean their infalling envelopes are still optically-thick and we do not expect to be able to see into the warmer inner regions surrounding these protostars. Note that these regions all show complicated, often bipolar, structures (see Figure 6) and that the sizes in this diagram refer

only to the central core of emission.

4.2. Size vs IRAS color

Leinert et al. (2004) found some evidence that the physical emission scale for the mid-infrared emission (in Herbig Ae stars) was correlated with the IRAS 12-25 micron color, defined as $-2.5 \log F_{\nu}(12\mu\text{m}) / F_{\nu}(25\mu\text{m})$. This is sensible since redder colors indicate cooler dust temperatures which naturally arise farther from the central star. Unfortunately, this diagram is difficult to use when your target sample spans a large luminosity range. This is because the radius for dust at given temperature depends on the root of central luminosity (see size-luminosity diagram above). Neither size-luminosity nor the size-color diagram can simultaneously take into account both of these effects. Liu et al. (2007) also explored mid-IR size differences as a function of the some SED parameters but his work also suffers from these same limitations.

Despite these drawbacks, we have produced a similar diagram as a way to present our basic results. Figure 9a shows our measured Gaussian FWHM size (in milliarcseconds) vs. the IRAS 12-25 color. We chose to use the distance-independent angular size instead of the physical size here, just so that our quantities did not depend on the uncertain distance estimates. Within each grouping, we do see some correlations. The Herbig Ae stars do show a correlation, with the striking result that nearly all the objects with colors bluer than 0.25 were unresolved by our survey. The embedded objects also might show a weak correlation. Just as the diagram in Leinert et al. (2004), this size-color diagram does not conserve a target’s position if you take the same disk temperature profile and change the luminosity. We only present this data to illustrate some trends within the sample, but caution against further use of this sort of diagram in subsequent work.

In order to overcome the luminosity and distance-dependencies for this sort of diagram, we introduce a new diagram in Figure 9b. Here plot the luminosity-normalized ring radius versus iras 12-25 color. This is defined as the physical ring radius (AU) divided by the square-root of luminosity (in solar luminosities). This quantity is both independent of distance and also naturally accounts for the expected scaling of emission scale with luminosity (for similar disk temperature profiles). Again, we see a significant correlation for the Herbig Ae stars, although other objects appear to scatter in this diagram. The location of each YSO system in this diagram is diagnostic of the disk flaring and temperature profiles and this diagram will prove useful for future work.

In the next paper in this series, we will be carrying out a radiative transfer study of YSO disks in order to understand the scatter in the size-luminosity diagram and how the deviations correlate with observables such as stellar luminosity and the [12]-[25] micron color. This new work will motivate improved diagrams to use for plotting basic observational data and will explore the potential for using luminosity-normalized sizes (radius AU / sqrt Luminosity) and surface-brightness relations.

5. Summary

We have presented a large survey of mid-infrared sizes of young stellar objects using the Keck Telescope. We can reliably resolve disks with size scales down to 35 mas (5 AU at 140pc), roughly $8\times$ smaller than the formal diffraction limit. We have overcome the traditional calibration problems that have plagued previous surveys by reconfiguring the Keck segments into multiple non-redundant interferometric arrays.

We have presented a detailed description of the experimental methodology and validated our calibration precision. We have measured the characteristic sizes of all our targets using a Gaussian + Halo model and have presented aperture synthesis imaging when possible. Our atlas of diffraction-limited imaging has revealed the complicated emissions around a sample of Class-I embedded YSOs and also discovered the remarkable photoevaporating circumbinary disk around MWC 361A.

Lastly, we have presented the most complete size – luminosity diagram for YSOs in the mid-infrared. Notably, we found the mid-IR size – luminosity relation shows a factor of 5-10 scatter for a given luminosity, much larger than the tight correlation seen in the near-infrared. This large scatter can partially be understood in terms of the influence of small dust grains that can be created in collisions between planetesimals in these young planet-forming disks (Tannirkulam et al. 2008). Disk clearing by binary companions and emission from remnant dust envelopes may also contribute to this scatter. With the help of a large grid of radiative transfer models, we will be fully exploring how the mid-infrared sizes correlate with disk properties in the next paper in the series.

While this particular experiment can no longer be carried out due to the absence of mid-IR instrumentation on the single Keck telescopes, we hope our method can be applied on current and future proposed segmented telescopes, such as the Gran Telescopio Canarias, the Cornell Caltech Atacama Telescope, and the Thirty-Meter Telescope.

We have appreciated the involvement of C.H. Townes in this project, especially for his contributions to the initial work. We give special thanks to Mark Kassis and Randy Campbell for superb observing assistance and helpful discussions concerning experimental details. We also thank Jayadev Rajagopal for his help at the telescope. We acknowledge partial support from NASA KPDA grant 1267021, NASA Origins grant NNG05GI80G, nsf-ast 0352728, and the NASA Michelson Fellowship program (MJI). This research has made use of the SIMBAD database, operated at CDS, Strasbourg, France. The data presented herein were obtained at the W.M. Keck Observatory, which is operated by Caltech, University of California and NASA. WMKO was made possible by the financial support of the W.M. Keck Foundation. The authors wish to recognize and acknowledge the very significant cultural role and reverence that the summit of Mauna Kea has always had within the indigenous Hawaiian community. We are most fortunate to have the opportunity to conduct observations from this mountain.

Facility: Keck:I (LWS)

REFERENCES

- Acke, B. & van den Ancker, M. E. 2004, *A&A*, 426, 151
- Akeson, R. L., Boden, A. F., Monnier, J. D., Millan-Gabet, R., Beichman, C., Beletic, J., Calvet, N., Hartmann, L., Hillenbrand, L., Koresko, C., Sargent, A., & Tannirkulam, A. 2005, *ApJ*, 635, 1173
- Araya, C., van der Blik, N., & Rodgers, B. 2007, in *Bulletin of the American Astronomical Society*, Vol. 38, *Bulletin of the American Astronomical Society*, 851–+
- Buscher, D. F. 1994, in *IAU Symp. 158: Very High Angular Resolution Imaging*, Vol. 158, 91–+
- Campbell, R. D. & Jones, B. 2004, *Advances in Space Research*, 34, 499
- Carmona, A., van den Ancker, M. E., & Henning, T. 2007, *A&A*, 464, 687
- Cohen, M., Biegging, J. H., Welch, W. J., & Dreher, J. W. 1985, *ApJ*, 292, 249
- Cordero, M. J., Thomas, S., van der Blik, N., Rodgers, B., Doppmann, G., & Sweet, A. 2006, in *Bulletin of the American Astronomical Society*, Vol. 38, *Bulletin of the American Astronomical Society*, 944–+
- Corporon, P. & Lagrange, A.-M. 1999, *A&AS*, 136, 429
- D’Alessio, P., Calvet, N., Hartmann, L., Franco-Hernández, R., & Servín, H. 2006, *ApJ*, 638, 314
- Danchi, W. C., Tuthill, P. G., & Monnier, J. D. 2001, *ApJ*, 562, 440
- Dullemond, C. P. & Dominik, C. 2004, *A&A*, 421, 1075
- Dullemond, C. P., Dominik, C., & Natta, A. 2001, *ApJ*, 560, 957
- Dyck, H. M., Simon, T., & Zuckerman, B. 1982, *ApJ*, 255, L103
- Eisner, J. A., Hillenbrand, L. A., White, R. J., Akeson, R. L., & Sargent, A. I. 2005, *ApJ*, 623, 952
- Gull, S. F. & Skilling, J. 1983, in *Indirect Imaging. Measurement and Processing for Indirect Imaging. Proceedings of an International Symposium held in Sydney, Australia, August 30-September 2, 1983*. Editor, J.A. Roberts; Publisher, Cambridge University Press, Cambridge, England, New York, NY, 1984. LC # QB51.3.E43 I53 1984. ISBN # 0-521-26282-8. P.267, 1983, 267+
- Haniff, C. A., Mackay, C. D., Titterton, D. J., Sivia, D., & Baldwin, J. E. 1987, *Nature*, 328, 694
- Hinz, P. M., Hoffmann, W. F., & Hora, J. L. 2001, *ApJ*, 561, L131

- Ireland, M. J., Monnier, J. D., & Thureau, N. 2006, in Presented at the Society of Photo-Optical Instrumentation Engineers (SPIE) Conference, Vol. 6268, *Advances in Stellar Interferometry*. Edited by Monnier, John D.; Schöller, Markus; Danchi, William C.. Proceedings of the SPIE, Volume 6268, pp. 62681T (2006).
- Ireland, M. J., Monnier, J. D., Tuthill, P. G., Cohen, R. W., De Buizer, J. M., Packham, C., Ciardi, D., Hayward, T., & Lloyd, J. P. 2007, *ApJ*, 662, 651
- Joint IRAS Science Working Group. 1988, in *IRAS Point Source Catalog (1988)*, 0–+
- Koresko, C. D., Beckwith, S., Ghez, A. M., Matthews, K., Herbst, T. M., & Smith, D. A. 1993, *AJ*, 105, 1481
- Lawson, P. R., Cotton, W. D., Hummel, C. A., Baron, F., Young, J. S., Kraus, S., Hofmann, K.-H., Weigelt, G. P., Ireland, M., Monnier, J. D., Thiébaud, E., Rengaswamy, S., & Chesneau, O. 2006, in Presented at the Society of Photo-Optical Instrumentation Engineers (SPIE) Conference, Vol. 6268, *Advances in Stellar Interferometry*. Edited by Monnier, John D.; Schöller, Markus; Danchi, William C.. Proceedings of the SPIE, Volume 6268, pp. 62681U (2006).
- Lawson, P. R., Cotton, W. D., Hummel, C. A., Monnier, J. D., Zhao, M., Young, J. S., Thorsteins-son, H., Meimon, S. C., Mugnier, L. M., Le Besnerais, G., Thiebaut, E. M., & Tuthill, P. G. 2004, in Presented at the Society of Photo-Optical Instrumentation Engineers (SPIE) Conference, Vol. 5491, *New Frontiers in Stellar Interferometry*, Proceedings of SPIE Volume 5491. Edited by Wesley A. Traub. Bellingham, WA: The International Society for Optical Engineering, 2004., p.886, ed. W. A. Traub, 886–+
- Leinert, C., Haas, M., Ábrahám, P., & Richichi, A. 2001, *A&A*, 375, 927
- Leinert, C., Richichi, A., & Haas, M. 1997, *A&A*, 318, 472
- Leinert, C., van Boekel, R., Waters, L. B. F. M., Chesneau, O., Malbet, F., Köhler, R., Jaffe, W., Ratzka, T., Dutrey, A., Preibisch, T., Graser, U., Bakker, E., Chagnon, G., Cotton, W. D., Dominik, C., Dullemond, C. P., Glazenborg-Kluttig, A. W., Glindemann, A., Henning, T., Hofmann, K.-H., de Jong, J., Lenzen, R., Ligi, S., Lopez, B., Meisner, J., Morel, S., Paresce, F., Pel, J.-W., Percheron, I., Perrin, G., Przygodda, F., Richichi, A., Schöller, M., Schuller, P., Stecklum, B., van den Ancker, M. E., von der Lühse, O., & Weigelt, G. 2004, *A&A*, 423, 537
- Liu, M. C., Graham, J. R., Ghez, A. M., Meixner, M., Skinner, C. J., Keto, E., Ball, R., Arens, J. F., & Jernigan, J. G. 1996, *ApJ*, 461, 334
- Liu, W. M., Hinz, P. M., Hoffmann, W. F., Brusa, G., Miller, D., & Kenworthy, M. A. 2005, *ApJ*, 618, L133

- Liu, W. M., Hinz, P. M., Meyer, M. R., Mamajek, E. E., Hoffmann, W. F., Brusa, G., Miller, D., & Kenworthy, M. A. 2007, *ApJ*, 658, 1164
- Mariñas, N., Telesco, C. M., Fisher, R. S., Packham, C., & Radomski, J. T. 2006, *ApJ*, 653, 1353
- Mathieu, R. D., Adams, F. C., & Latham, D. W. 1991, *AJ*, 101, 2184
- McCarthy, D. W. 1982, *ApJ*, 257, L93
- Millan-Gabet, R., Malbet, F., Akeson, R., Leinert, C., Monnier, J., & Waters, R. 2007, in *Protostars and Planets V*, ed. B. Reipurth, D. Jewitt, & K. Keil, 539–554
- Millan-Gabet, R. & Monnier, J. D. 2002, *ApJ*, 580, L167
- Millan-Gabet, R., Schloerb, F. P., & Traub, W. A. 2001, *ApJ*, 546, 358
- Millan-Gabet, R., Schloerb, F. P., Traub, W. A., Malbet, F., Berger, J. P., & Bregman, J. D. 1999, *ApJ*, 513, L131
- Monnier, J. D., Berger, J.-P., Millan-Gabet, R., Traub, W. A., Schloerb, F. P., Pedretti, E., Benisty, M., Carleton, N. P., Hagenauer, P., Kern, P., Labeye, P., Lacasse, M. G., Malbet, F., Perraut, K., Pearlman, M., & Zhao, M. 2006, *ApJ*, 647, 444
- Monnier, J. D. & Millan-Gabet, R. 2002, *ApJ*, 579, 694
- Monnier, J. D., Millan-Gabet, R., Billmeier, R., Akeson, R. L., Wallace, D., Berger, J.-P., Calvet, N., D’Alessio, P., Danchi, W. C., Hartmann, L., Hillenbrand, L. A., Kuchner, M., Rajagopal, J., Traub, W. A., Tuthill, P. G., Boden, A., Booth, A., Colavita, M., Gathright, J., Hrynevych, M., Le Mignant, D., Ligon, R., Neyman, C., Swain, M., Thompson, R., Vasisht, G., Wizinowich, P., Beichman, C., Beletic, J., Creech-Eakman, M., Koresko, C., Sargent, A., Shao, M., & van Belle, G. 2005, *ApJ*, 624, 832
- Monnier, J. D., Tannirkulam, A., Tuthill, P. G., Ireland, M., Cohen, R., Danchi, W. C., & Baron, F. 2008, *ApJ*, 681, L97
- Monnier, J. D., Tuthill, P. G., & Danchi, W. C. 1999a, *ApJ*, 525, L97
- Monnier, J. D., Tuthill, P. G., Danchi, W. C., Murphy, N., & Harries, T. J. 2007, *ApJ*, 655, 1033
- Monnier, J. D., Tuthill, P. G., Lopez, B., Cruzalebes, P., Danchi, W. C., & Haniff, C. A. 1999b, *ApJ*, 512, 351
- Narayan, R. & Nityananda, R. 1986, *ARA&A*, 24, 127
- Natta, A., Prusti, T., Neri, R., Wooden, D., Grinin, V. P., & Mannings, V. 2001, *A&A*, 371, 186
- Pauls, T. A., Young, J. S., Cotton, W. D., & Monnier, J. D. 2005, *PASP*, 117, 1255

- Perrin, G., Coude Du Foresto, V., Ridgway, S. T., Mariotti, J.-M., Traub, W. A., Carleton, N. P., & Lacasse, M. G. 1998, *A&A*, 331, 619
- Perrin, M. 2006, PhD thesis, University of California at Berkeley
- Quanz, S. P., Henning, T., Bouwman, J., Ratzka, T., & Leinert, C. 2006, *ApJ*, 648, 472
- Rajagopal, J., Menut, J.-L., Wallace, D., Danchi, W. C., Chesneau, O., Lopez, B., Monnier, J. D., Ireland, M., & Tuthill, P. G. 2007, *ApJ*, 671, 2017
- Sivia, D. 1987, PhD thesis, Cambridge University
- Skemer, A. J., Close, L. M., Hinz, P. M., Hoffmann, W. F., Kenworthy, M. A., & Miller, D. L. 2008, *ApJ*, 676, 1082
- Skrutskie, M. F., Cutri, R. M., Stiening, R., Weinberg, M. D., Schneider, S., Carpenter, J. M., Beichman, C., Capps, R., Chester, T., Elias, J., Huchra, J., Liebert, J., Lonsdale, C., Monet, D. G., Price, S., Seitzer, P., Jarrett, T., Kirkpatrick, J. D., Gizis, J. E., Howard, E., Evans, T., Fowler, J., Fullmer, L., Hurt, R., Light, R., Kopan, E. L., Marsh, K. A., McCallon, H. L., Tam, R., Van Dyk, S., & Wheelock, S. 2006, *AJ*, 131, 1163
- Smith, K. W., Balega, Y. Y., Duschl, W. J., Hofmann, K.-H., Lachaume, R., Preibisch, T., Schertl, D., & Weigelt, G. 2005, *A&A*, 431, 307
- Stark, C. C., Kuchner, M. J., Traub, W. A., Monnier, J. D., Serabyn, E., & Colavita, M. 2009, in *American Astronomical Society Meeting Abstracts*, Vol. 213, American Astronomical Society Meeting Abstracts, #358.01–+
- Tannirkulam, A., Harries, T. J., & Monnier, J. D. 2007, *ApJ*, 661, 374
- Tannirkulam, A., Monnier, J. D., Harries, T. J., Millan-Gabet, R., Zhu, Z., Pedretti, E., Ireland, M., Tuthill, P., ten Brummelaar, T., McAlister, H., Farrington, C., Goldfinger, P. J., Sturmman, J., Sturmman, L., & Turner, N. 2008, *ApJ*, 689, 513
- Thomas, S. J., van der Blik, N. S., Rodgers, B., Doppmann, G., & Bouvier, J. 2007, in *IAU Symposium*, Vol. 240, *IAU Symposium*, ed. W. I. Hartkopf, E. F. Guinan, & P. Harmanec, 250–253
- Tuthill, P. G., Monnier, J. D., & Danchi, W. C. 1999, *Nature*, 398, 487
- . 2001, *Nature*, 409, 1012
- Tuthill, P. G., Monnier, J. D., Danchi, W. C., Hale, D. D. S., & Townes, C. H. 2002, *ApJ*, 577, 826
- Tuthill, P. G., Monnier, J. D., Danchi, W. C., Wishnow, E. H., & Haniff, C. A. 2000, *PASP*, 112, 555

- van Boekel, R., Dullemond, C. P., & Dominik, C. 2005, *A&A*, 441, 563
- van Boekel, R., Min, M., Leinert, C., Waters, L. B. F. M., Richichi, A., Chesneau, O., Dominik, C., Jaffe, W., Dutrey, A., Graser, U., Henning, T., de Jong, J., Köhler, R., de Koter, A., Lopez, B., Malbet, F., Morel, S., Paresce, F., Perrin, G., Preibisch, T., Przygodda, F., Schöller, M., & Wittkowski, M. 2004, *Nature*, 432, 479
- Wang, H., Apai, D., Henning, T., & Pascucci, I. 2004, *ApJ*, 601, L83
- Weiner, J., Tatebe, K., Hale, D. D. S., Townes, C. H., Monnier, J. D., Ireland, M., Tuthill, P. G., Cohen, R., Barry, R. K., Rajagopal, J., & Danchi, W. C. 2006, *ApJ*, 636, 1067
- Zhao, M., Gies, D., Monnier, J. D., Thureau, N., Pedretti, E., Baron, F., Merand, A., ten Brummelaar, T., McAlister, H., Ridgway, S. T., Turner, N., Sturmann, J., Sturmann, L., Farrington, C., & Goldfinger, P. J. 2008, *ApJ*, 684, L95

Table 1. Observing Log

Target	U.T.		Calibrator Names ^a
	Date	Time	
51 Oph	2005 May 26	10:05	σ Lib
	2005 May 26	10:20	σ Lib, v3879 Sgr
AB Aur	2004 Aug 30	15:12	<i>i</i> Aur
	2004 Aug 30	15:34	<i>i</i> Aur
	2004 Aug 31	15:29	<i>i</i> Aur
	2004 Sep 01	15:37	<i>i</i> Aur
AFGL 2136	2005 May 26	12:47	v3879 Sgr
	2005 May 26	13:06	v3879 Sgr
AFGL 2591	2004 Sep 01	09:01	X Oph
	2004 Sep 01	09:28	X Oph
AFGL 490	2004 Sep 01	12:23	α Tau
	2004 Sep 01	12:40	α Cas
FU Ori	2005 Feb 20	07:28	<i>i</i> Aur
	2005 Feb 20	08:33	<i>i</i> Aur
GW Ori	2005 Feb 20	07:14	<i>i</i> Aur
	2005 Feb 20	08:22	α Tau, <i>i</i> Aur
HD 142527	2005 May 26	08:32	GM Lup
	2005 May 26	09:12	GM Lup
HD 142666	2005 May 26	09:49	σ Lib
	2005 May 26	10:11	σ Lib
HD 144432	2005 May 26	08:56	GM Lup
	2005 May 26	09:42	σ Lib
HD 41511	2005 Feb 20	05:24	α CMa
	2005 Feb 20	09:21	α CMa
HD 45677	2005 Feb 19	07:32	α CMa, α Tau
	2005 Feb 19	07:32	α CMa, α Tau
	2005 Feb 19	09:08	α CMa
HD 50138	2005 Feb 20	05:50	α CMa
	2005 Feb 20	09:16	α CMa
LkH α 101	2004 Aug 30	14:45	α Tau, <i>i</i> Aur
	2004 Aug 31	14:56	α Tau, <i>i</i> Aur
	2004 Sep 01	15:33	<i>i</i> Aur
	2005 Feb 19	07:00	α Tau
LkH α 234	2005 May 26	14:54	MO Cep
	2005 May 26	15:11	MO Cep
MWC 1080	2004 Sep 01	13:25	α Cas, MO Cep
	2004 Sep 01	13:28	α Cas, MO Cep
MWC 147	2005 Feb 20	05:59	α CMa, α Tau
	2005 Feb 20	08:54	α CMa
MWC 275	2004 Sep 01	06:33	v3879 Sgr
	2004 Sep 01	06:46	v3879 Sgr
MWC 297	2004 Aug 30	09:24	v3879 Sgr
	2004 Aug 31	07:39	v3879 Sgr
MWC 300	2004 Aug 31	07:44	v3879 Sgr
	2004 Aug 31	07:55	v3879 Sgr

Table 1—Continued

Target	U.T.		Calibrator Names ^a
	Date	Time	
MWC 342	2004 Aug 31	10:15	XI Cyg
	2004 Aug 31	10:43	XI Cyg, v1339 Cyg
MWC 349	2004 Aug 31	10:10	XI Cyg
	2004 Aug 31	10:53	XI Cyg, v1339 Cyg
MWC 361	2005 May 26	14:48	MO Cep
	2005 May 26	15:03	MO Cep
MWC 480	2004 Aug 31	15:06	<i>i</i> Aur
	2004 Aug 31	15:10	<i>i</i> Aur
	2004 Aug 31	15:54	α Tau, <i>i</i> Aur
	2004 Aug 31	15:58	α Tau, <i>i</i> Aur
MWC 614	2004 Sep 01	15:06	<i>i</i> Aur
	2004 Aug 31	09:02	γ Aql
	2004 Aug 31	09:23	γ Aql, R Lyr
MWC 863	2004 Sep 01	05:47	η Sgr, v3879 Sgr
	2004 Sep 01	06:08	η Sgr, v3879 Sgr
Mon R2 IRS 3	2005 Feb 19	07:48	α CMa
	2005 Feb 19	09:28	α CMa
RY Tau	2004 Aug 31	15:16	α Tau
	2004 Aug 31	15:18	α Tau
	2004 Aug 31	15:49	α Tau
	2004 Sep 01	15:11	<i>i</i> Aur
R CrA	2004 Aug 31	06:16	η Sgr
	2004 Aug 31	06:34	η Sgr
R Mon	2005 Feb 20	05:30	α CMa
	2005 Feb 20	05:33	α CMa
	2005 Feb 20	09:03	α CMa
S140 IRS1	2004 Sep 01	11:30	MO Cep
	2004 Sep 01	11:49	MO Cep
T Tau	2005 Feb 20	06:39	α Tau, <i>i</i> Aur
	2005 Feb 20	07:50	α Tau, <i>i</i> Aur
Z CMa	2005 Feb 19	07:56	α CMa
	2005 Feb 19	09:33	α CMa
v1295 Aql	2005 May 26	14:04	γ Aql
	2005 May 26	14:19	γ Aql
v1685 Cyg	2004 Aug 31	09:32	γ Aql
	2004 Aug 31	10:58	XI Cyg, v1339 Cyg
	2004 Aug 31	11:02	XI Cyg, v1339 Cyg
	2004 Sep 01	09:52	v1339 Cyg
v376 Cas	2004 Sep 01	11:25	α Cas
	2004 Sep 01	11:44	α Cas
v645 Cyg	2004 Aug 30	11:28	β And, γ Aql, R Lyr
	2004 Aug 31	10:38	XI Cyg, v1339 Cyg
	2004 Aug 31	11:19	XI Cyg, v1339 Cyg
v883 Ori	2005 Feb 19	07:38	α Tau
	2005 Feb 19	09:17	α CMa

Table 1—Continued

Target	U.T.		Calibrator Names ^a
	Date	Time	
v892 Tau	2004 Aug 31	14:46	α Tau, <i>i</i> Aur
	2004 Aug 31	14:51	α Tau, <i>i</i> Aur
	2004 Aug 31	15:34	α Tau
	2004 Aug 31	15:39	α Tau
	2004 Sep 01	14:58	α Cet
	2005 Feb 19	07:07	α Tau

^aAll data taken using Pattern 6 (see §2.1). All calibrators were assumed to be as unresolved except for α Tau with UD diameter 19.8 mas (Perrin et al. 1998).

Table 2. Source List

Target	Alternate Name	J2000 Coordinates ^a		V ^b	J	H	K	10.7 μ m Jy ^c	IRAS12 Jy ^d	IRAS25 Jy	Binary? (Ref ^e)
		α	δ								
Embedded Young Stars (Class I Sources)											
AFGL 490		03 27 38.77	+58 47 00.1	–	10.9	8.1	5.7	58.3 \pm 5.8	82.4	278.0	N
Mon R2 IRS 3		06 07 47.86	–06 22 56.0	–	13.2	9.8	6.6	109.9 \pm 11.0	470.0	4100.0	Y (1)
AFGL 2136		18 22 26.38	–13 30 12.0	–	15.0	12.7	7.3	37.1 \pm 3.7	155.0	574.0	N
AFGL 2591		20 29 24.87	+40 11 19.4	–	14.3	10.8	6.6	127.7 \pm 12.8	439.0	1110.0	N
S140 IRS1		22 19 18.28	+63 18 45.8	–	12.3	9.3	6.1	125.1 \pm 12.5	308.0	1540.0	N
Herbig Ae Stars											
AB Aur	HD 31293	04 55 45.83	+30 33 04.4	7.1	5.9	5.1	4.2	28.3 \pm 2.8	27.2	48.1	N
MWC 480	HD 31648	04 58 46.26	+29 50 37.1	7.7	6.9	6.3	5.5	15.4 \pm 1.5	10.2	10.3	N
HD 142666	v1026 Sco	15 56 40.02	–22 01 40.0	8.8	7.4	6.7	6.1	5.9 \pm 0.6	8.6	11.2	N
HD 142527		15 56 41.89	–42 19 23.3	8.3	6.5	5.7	5.0	11.1 \pm 1.1	10.4	21.2	N
HD 144432		16 06 57.95	–27 43 09.4	8.2	7.1	6.5	5.9	9.8 \pm 1.0	7.5	9.4	Y (2)
MWC 863	HD 150193	16 40 17.92	–23 53 45.2	8.9	6.9	6.2	5.5	18.9 \pm 3.8	17.6	18.1	Y (3)
51 Oph	HD 158632	17 31 24.97	–23 57 45.3	4.8	4.9	4.7	4.3	16.9 \pm 1.7	15.7	10.2	N
MWC 275	HD 163296	17 56 21.29	–21 57 21.8	6.9	6.2	5.5	4.8	15.3 \pm 1.5	18.2	21.0	N
R CrA		19 01 53.68	–36 57 08.2	11.5	6.9	5.0	2.9	110.8 \pm 11.1	111.0	222.0	N
MWC 614	HD 179218	19 11 11.24	+15 47 15.6	7.2	7.0	6.6	6.0	20.6 \pm 4.0	23.4	43.6	N
v1295 Aql	HD 190973	20 03 02.51	+05 44 16.7	7.8	7.2	6.6	5.9	6.8 \pm 0.7	7.2	5.5	N
Herbig Be Stars											
v376 Cas		00 11 26.52	+58 50 03.7	15.6	11.0	8.4	6.3	21.1 \pm 2.1	33.0	88.1	N
v892 Tau	Elias 1	04 18 40.62	+28 19 15.5	15.3	8.7	7.0	5.8	34.1 \pm 3.9	33.2	99.9	Y (4)
LkH α 101		04 30 14.44	+35 16 24.0	15.7	8.3	5.6	3.0	289.7 \pm 29.0	362.0	340.0	Y (5)
v883 Ori	IRAS 05358-0704	05 38 18.10	–07 02 25.9	14.4	9.3	6.8	5.2	39.8 \pm 6.0	52.5	127.0	N
MWC 147	HD 259431	06 33 05.20	+10 19 19.9	8.8	7.5	6.7	5.7	10.0 \pm 1.0	12.5	20.2	Y (6)
R Mon		06 39 09.95	+08 44 09.7	10.4	9.7	8.0	6.4	42.8 \pm 4.3	54.7	132.0	Y (7)
Z CMa		07 03 43.17	–11 33 06.3	9.9	6.5	5.2	3.8	144.7 \pm 14.5	127.0	221.0	Y (8)
MWC 297	NZ Ser	18 27 39.53	–03 49 52.1	12.3	6.1	4.4	3.0	84.7 \pm 8.5	159.0	224.0	N
v1685 Cyg	MWC 340	20 20 28.25	+41 21 51.5	10.7	7.9	6.8	5.8	4.6 \pm 0.8	–	–	Y (9)
MWC 349	v1478 Cyg	20 32 45.53	+40 39 36.6	13.2	6.2	4.8	3.2	153.9 \pm 37.9	179.0	112.0	Y (10)
MWC 361	HD 200775	21 01 36.91	+68 09 47.7	7.4	6.1	5.5	4.7	8.2 \pm 0.8	26.7	76.8	Y (11)
v645 Cyg	AFGL 2789	21 39 58.25	+50 14 20.9	13.6	10.9	9.2	6.8	57.4 \pm 12.0	114.0	219.0	N
LkH α 234		21 43 06.82	+66 06 54.2	11.9	9.5	8.2	7.1	3.9 \pm 0.4	14.8	79.0	Y (12)
MWC 1080	v628 Cas	23 17 25.59	+60 50 43.6	11.6	7.5	6.0	4.8	15.5 \pm 1.8	22.2	25.1	Y (3)
Emission-line Stars of Uncertain Classification (possible Herbig, B[e] stars, or other)											
HD 41511		06 04 59.13	–16 29 03.9	5.0	2.9	2.1	1.7	208.7 \pm 20.9	144.0	72.2	N
HD 45677		06 28 17.42	–13 03 11.0	8.1	7.2	6.3	4.8	181.9 \pm 28.1	146.0	143.0	N
HD 50138		06 51 33.41	–06 57 59.2	6.6	5.9	5.1	4.1	94.6 \pm 9.5	70.3	62.5	N
MWC 300	v431 Sct	18 29 25.70	–06 04 37.2	10.5	9.3	8.2	6.2	64.6 \pm 6.5	101.0	113.0	Y (3)
MWC 342	v1972 Cyg	20 23 03.61	+39 29 49.9	10.6	7.0	5.8	4.7	51.5 \pm 13.5	46.2	48.6	N
T Tauri Stars											
RY Tau		04 21 57.40	+28 26 35.5	10.2	7.2	6.1	5.4	14.4 \pm 1.4	17.5	26.1	N
T Tau		04 21 59.43	+19 32 06.4	9.6	7.2	6.2	5.3	10.7 \pm 1.1	14.9	44.2	Y (13)
GW Ori		05 29 08.39	+11 52 12.6	9.9	7.7	7.1	6.6	10.0 \pm 1.0	7.9	20.5	Y (14)
FU Orionis Objects											
FU Ori		05 45 22.36	+09 04 12.4	8.9	6.5	5.7	5.2	5.9 \pm 0.6	5.9	14.1	Y (15)

^aCoordinates and JHK magnitudes are from 2MASS (Skrutskie et al. 2006).

^bV band magnitudes from SIMBAD.

^cFlux included within aperture of diameter of 3'' and was derived from this work.

^dIRAS12 and IRAS25 fluxes are from IRAS point source catalog (Joint IRAS Science Working Group 1988) using broadband filters from 8-15 μm and 15-30 μm .

^eBinary references: 1. Koresko et al. (1993). 2. Carmona et al. (2007). 3. Corporon & Lagrange (1999). 4. Smith et al. (2005). 5. Tuthill et al. (2001). 6. Araya et al. (2007). 7. Thomas et al. (2007). 8. Millan-Gabet & Monnier (2002). 9. Cordero et al. (2006). 10. Cohen et al. (1985). 11. Monnier et al. (2006). 12. Leinert et al. (1997). 13. Dyck et al. (1982). 14. Mathieu et al. (1991). 15. Wang et al. (2004).

Table 3. 1-D and 2-D Characteristic Sizes at $10.7\mu\text{m}$

Target	1-D Gaussian ^a			2-D Gaussian ^b				χ^2_ν	Comments	
	FWHM mas	Halo (%)	χ^2_ν	FWHM (mas)		PA deg	Halo (%)			
				Major	Minor					
Embedded Young Stars (Class I Sources)										
AFGL 490	100± 5	11±3	7.0	110± 4	81± 3	20± 2	12±2	2.4	Faint extension to South	
Mon R2 IRS 3	108±16	39±6	20.0	144± 6	88± 5	41± 2	35±2	6.1	Nebulosity and binary at $\rho = 836$ mas, $\theta = 16.7^\circ$	
AFGL 2136	120± 3	20±2	2.1	125± 5	115± 3	44± 14	19±2	1.7	Faint extension to West-Southwest	
AFGL 2591	118± 3	9±4	4.2	123± 3	111± 3	114± 7	9±4	3.4	Nebulosity to West	
S140 IRS1	134± 3	40±1	5.5	136± 5	133± 4	117± 25	40±2	5.6	Extensive nebulosity to South	
Herbig Ae Stars										
AB Aur	70± 3	11±1	0.4	72± 3	68± 6	27± 25	11±1	0.4	Slight extension PA~30° but mostly symmetrical	
MWC 480	16±20	3±2	0.8	29±24	0±17	29± 32	2±2	0.8		
HD 142666	33±24	4±2	0.6	65±65	0±40	173± 56	2±4	0.5		
HD 142527	50± 6	3±1	0.4	55± 8	45± 4	60± 22	3±1	0.4		
HD 144432	39± 5	0±1	1.0	49±14	25±25	103± 31	0±1	0.9		
MWC 863	21±21	2±2	1.0	33± 6	8±14	12± 21	2±1	0.9		
51 Oph	0± 4	0±1	0.3	0±27	0± 1	93± 53	0±1	0.3		
MWC 275	17±16	4±3	1.2	24±24	8± 9	60± 51	4±3	1.2		
R CrA	69± 2	10±1	0.9	77± 2	64± 2	78± 4	10±1	0.6		
MWC 614	68± 4	4±1	0.7	80± 3	52± 8	17± 9	4±1	0.3		
v1295 Aql	8±15	0±1	0.5	34±34	0± 1	22± 49	0±1	0.5		
Herbig Be Stars										
v376 Cas	37± 3	1±2	0.5	40± 3	33± 5	134± 25	1±2	0.5		Resolved circumbinary disk
v892 Tau	210± 8	0±3	21.6	244± 6	123± 9	49± 1	0±2	2.1		
LkH α 101	70± 3	4±2	0.8	73± 2	62± 9	180± 14	4±2	0.6	Slight extension North-South	
v883 Ori	43± 4	6±2	0.9	46± 4	37±10	110± 31	7±3	0.9		
MWC 147	24±14	3±5	0.6	37±14	0±11	52± 31	3±7	0.6	Mostly circularly symmetric Faint extension toward companion along PA~128°	
R Mon	94± 2	8±1	0.7	97± 4	91± 2	66± 23	8±1	0.7		
Z CMa	61± 4	1±1	2.4	68± 2	41± 6	137± 5	2±1	0.6		
MWC 297	55± 6	2±1	1.2	59± 9	50± 6	40± 21	2±1	1.1		
v1685 Cyg	29±17	12±6	0.6	56±23	19±19	112± 26	11±6	0.5		
MWC 349	81± 6	8±3	4.0	94± 7	26±15	95± 6	8±3	1.1		
MWC 361	45±17	45±2	0.3	55±14	39±30	17± 26	45±2	0.3		
v645 Cyg	46±11	5±4	1.0	55± 4	38±19	34± 16	5±4	0.9		
LkH α 234	27±19	6±1	0.2	42±42	0±44	91± 34	6±2	0.2		
MWC 1080	0±10	17±3	8.1	0±44	0± 1	115± 49	17±2	8.4		
Emission-line Stars of Uncertain Classification (possible Herbig, B[e] stars, or other)										
HD 41511	0± 6	0±2	1.6	19±26	9± 9	36± 90	0±2	1.7		
HD 45677	70± 3	12±1	1.0	77± 3	66± 3	70± 5	12±1	0.7		
HD 50138	58± 6	1±1	1.4	66± 4	46± 9	63± 6	1±1	1.0		
MWC 300	49± 3	1±1	0.6	57± 4	44± 2	35± 14	0±1	0.4		
MWC 342	38±22	6±1	1.0	39±11	37±37	107± 90	6±2	1.0		
T Tauri Stars										
RY Tau	49± 4	2±1	0.9	59±10	37±25	12± 45	2±3	0.8	Binary: $\rho = 639$ mas, $\theta = -170.9^\circ$	
T Tau	0±13	27±2	3.5	29±21	0± 7	1± 31	26±2	3.6		
GW Ori	37±20	0±2	0.7	54± 7	25±29	107± 10	0±5	0.6		
FU Orionis Objects										

Table 3—Continued

Target	1-D Gaussian ^a			2-D Gaussian ^b				Comments	
	FWHM mas	Halo (%)	χ^2_ν	FWHM (mas)		PA deg	Halo (%)		χ^2_ν
				Major	Minor				
FU Ori	21±22	10±5	1.2	55±27	0±13	65± 35	8±4	1.2	Binary: $\rho = 488$ mas, $\theta = 163.3^\circ$

^aParameters of 1-dimensional Gaussian fits: Full-width at half-maximum (FWHM) in milliarcseconds (mas), percentage of light coming from “halo” on scales larger than $\sim 0.5''$.

^bParameters of 2-dimensional Gaussian fits: Full-width at half-maximum (FWHM) along major and minor axes respectively, Position angle (PA) of major axis in degrees East of North, percentage of light coming from extended “halo.”

Image Positions on Sky

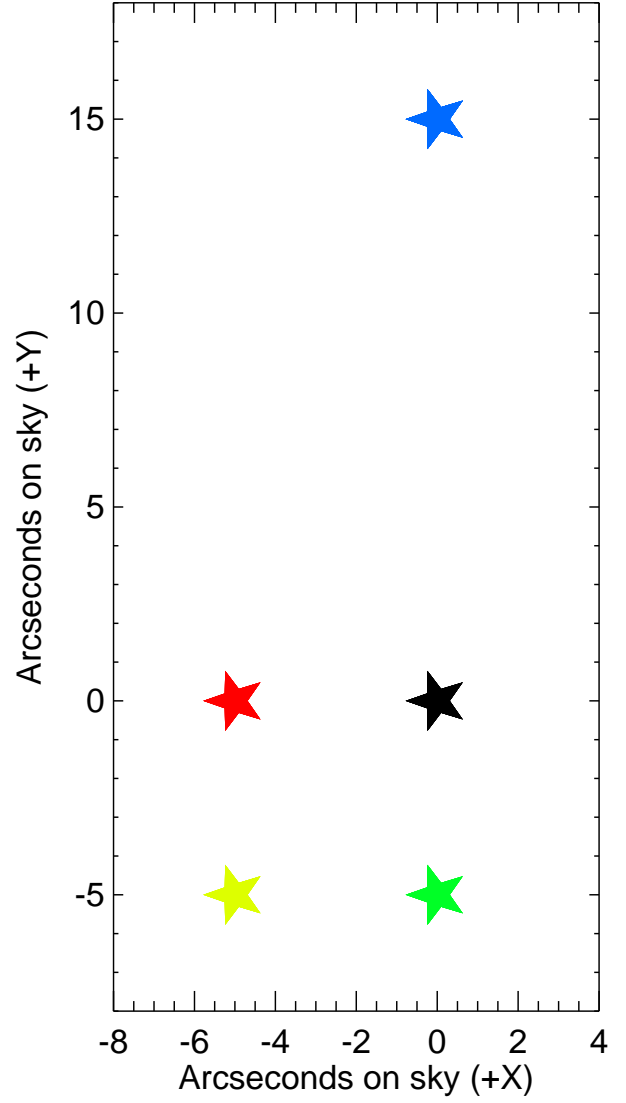
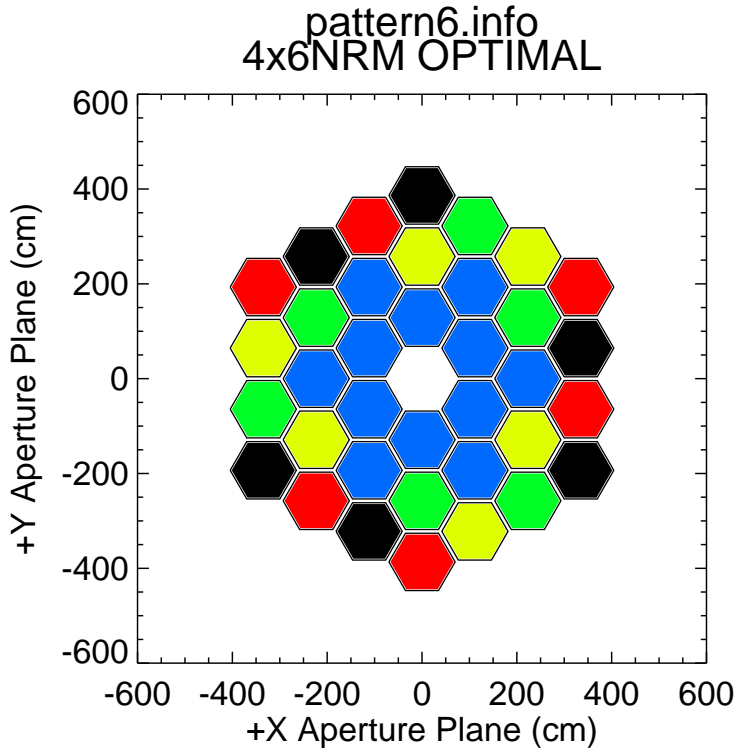


Fig. 1.— (left panel) a. This figure shows the 36 segments of the Keck telescope, color-coded by the tilt imposed using the Keck Active Control System (ACS) for “pattern 6” described in §2.1. (right panel) b. This figure shows the image plane locations associated with the tilts color-coded in panel (a). The 10'' X 10'' array detector can simultaneously record fringe patterns of the bottom four image plane locations, while the top image is off the chip.

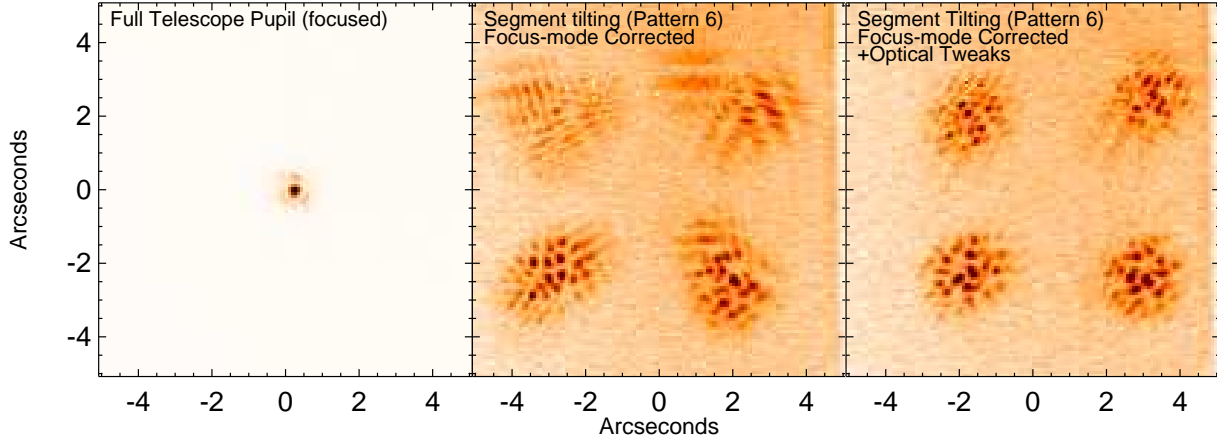


Fig. 2.— (*left panel*) a. This figure shows a single frame (90 ms exposure) of a calibrator source using the full pupil and after careful focusing. Although this image is “diffraction-limited,” there are significant variations of this PSF with time and seeing conditions and the first Airy ring is usually distorted by phase aberrations. (*middle panel*) b. After applying the tilts and pistons for pattern 6 (see Figure 1), we see the light from the star is split into four patterns of overlapping fringes. This image was taken after correcting for “focus mode” introduced when changing sensor gain setting (see discussion in §2.2). Note the large residual tilt errors on some segments in the top of the image frame. (*right panel*) c. The tilt errors from the middle panel were analyzed at the beginning of the observing night and perturbative “optical tweaks” were applied to the segment actuators. The resulting image quality is much improved, showing four interference patterns with well-aligned segments. The intensity patterns are all displayed with a linear scale.

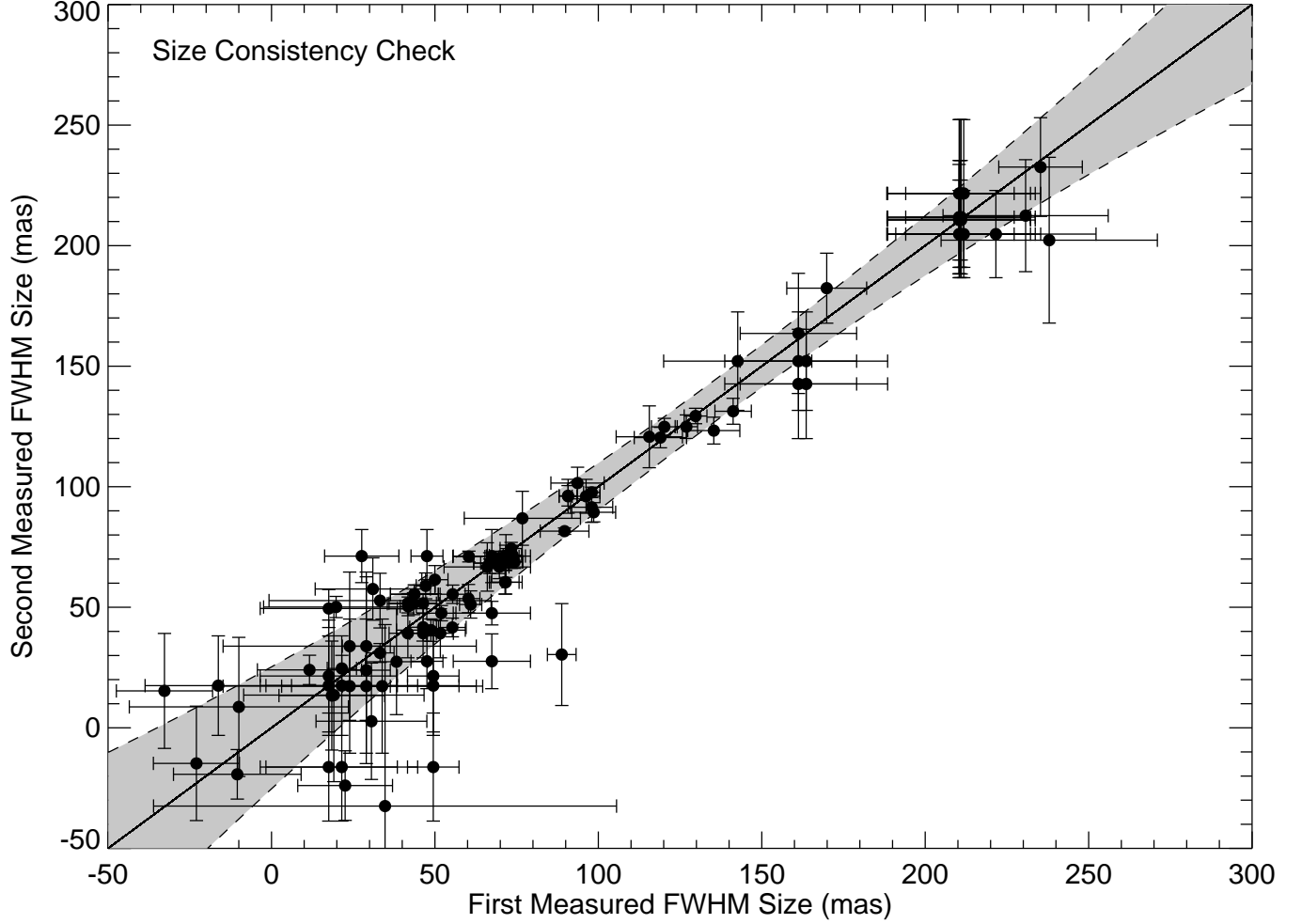


Fig. 3.— Nearly all the targets of the Keck segment-tilting experiment were observed multiply times under independent observing conditions – this was a core design principle of our observing methodology. Here we plot the measured size (Gaussian FWHM) at one epoch versus another in order to estimate systematic errors as a function of the target size. Here we see extremely good self-consistency within reported errors and the typical 1-sigma confidence limits for the mean diameter are shown in the central grey-shaded region. We can reliably (with 2-sigma confidence) estimate partially-resolved objects down to a full-width at half-maximum of ~ 35 milliarcseconds, about $10\times$ smaller than the formal diffraction limit.

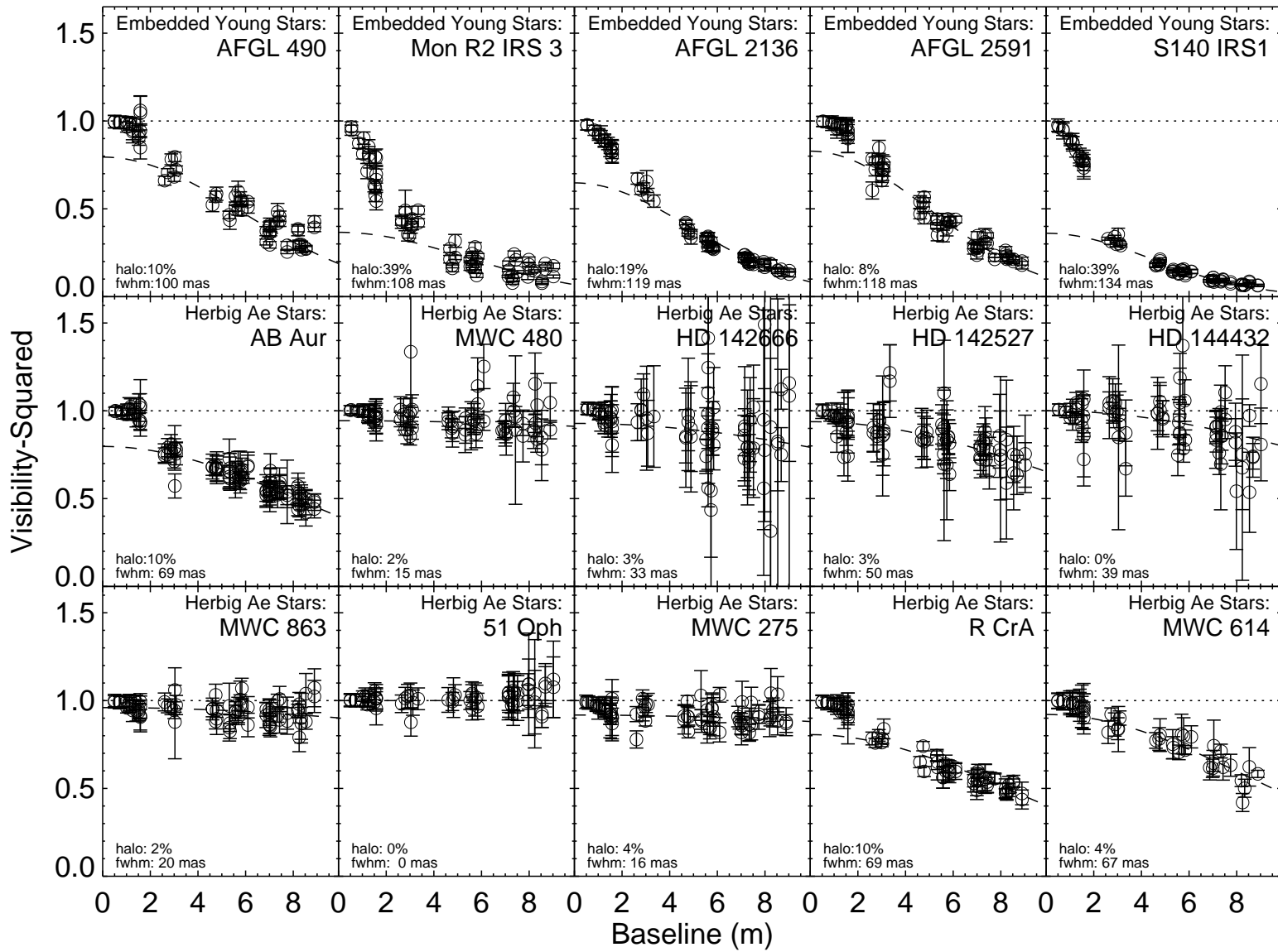


Fig. 4.— Here we present all the squared-visibility data as a function baseline in meters. For all stars the observing wavelength was $10.7\mu\text{m}$. For this presentation, we present each epoch separately and have performed averaging in the (u,v) plane with a smoothing length of 0.45 m . Additionally, we have overplotted the best-fit circular Gaussian fit and the parameters appear inside each frame for reference. See §3.2 for more details on the fitting procedure

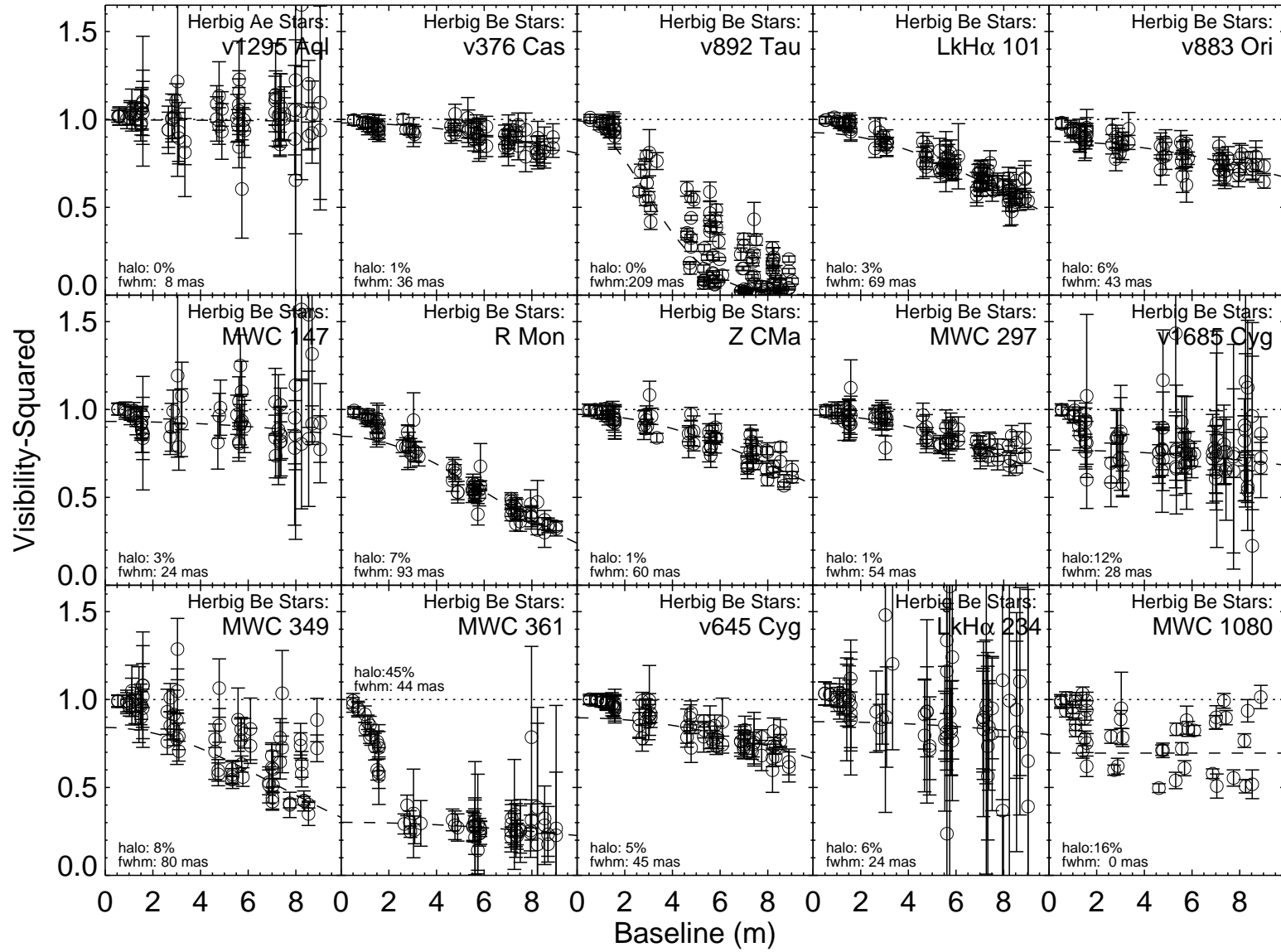


Figure 4 (continued)

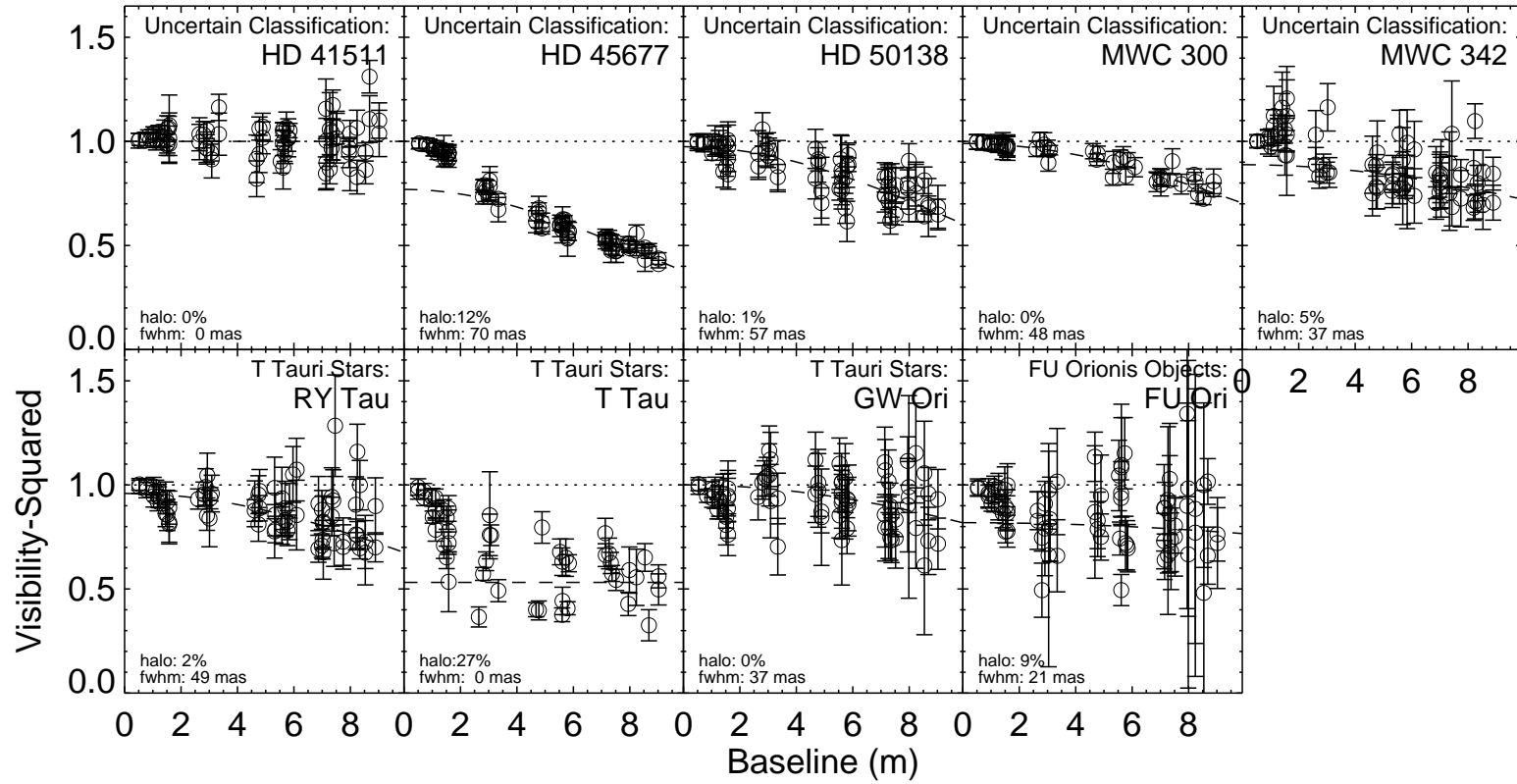


Figure 4 (continued)

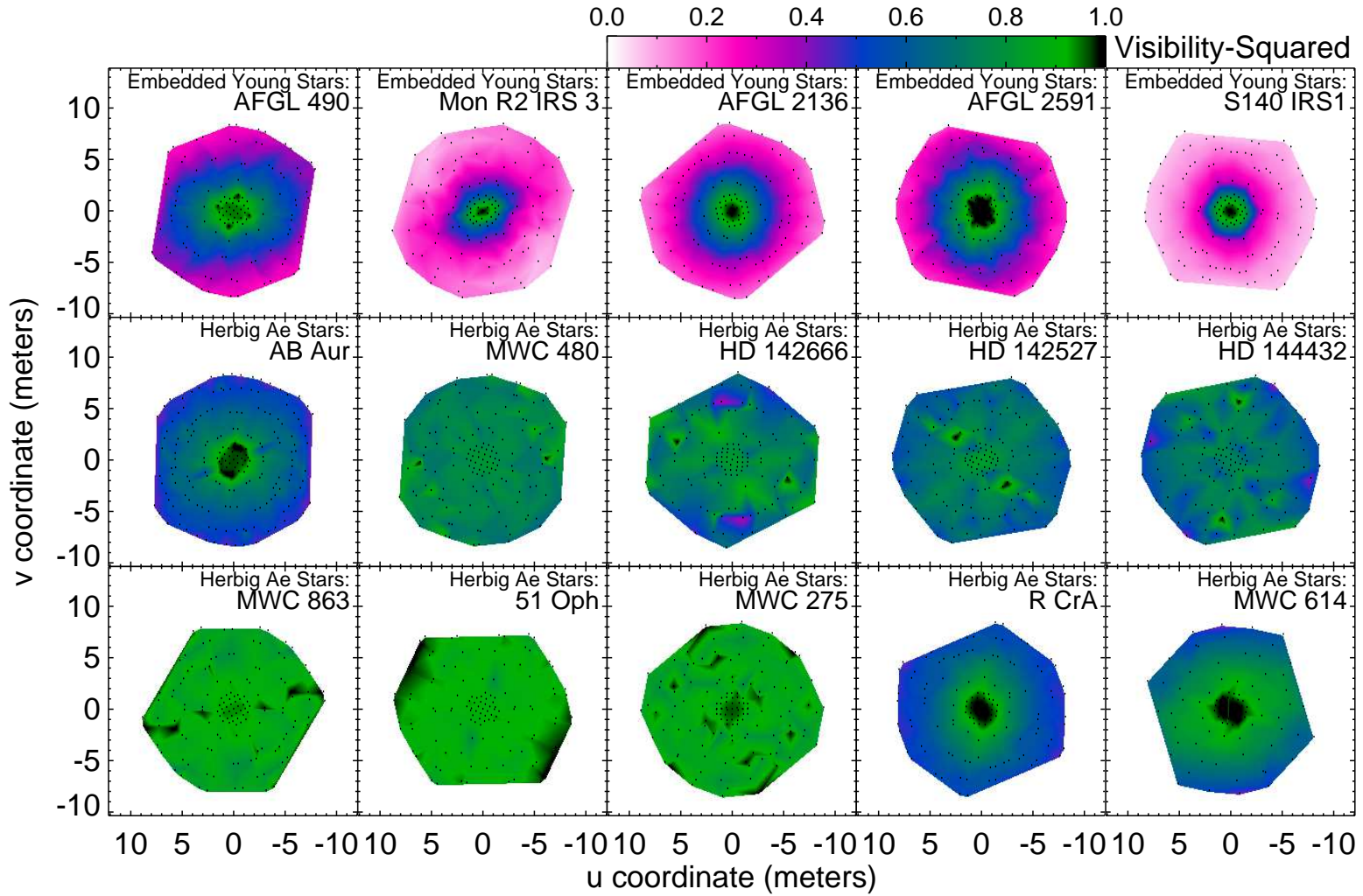


Fig. 5.— Here we present all the squared-visibility data as 2-dimensional function of the (u, v) coordinates. As for the previous figure, we have averaged on scale of 0.45 meters. The visibility data is interpolated onto the grid and shown in color while the black dots show the actual locations of the uv datapoints. The intensity scale can found at the top in order to translate the color scale into quantitative values of squared-visibility.

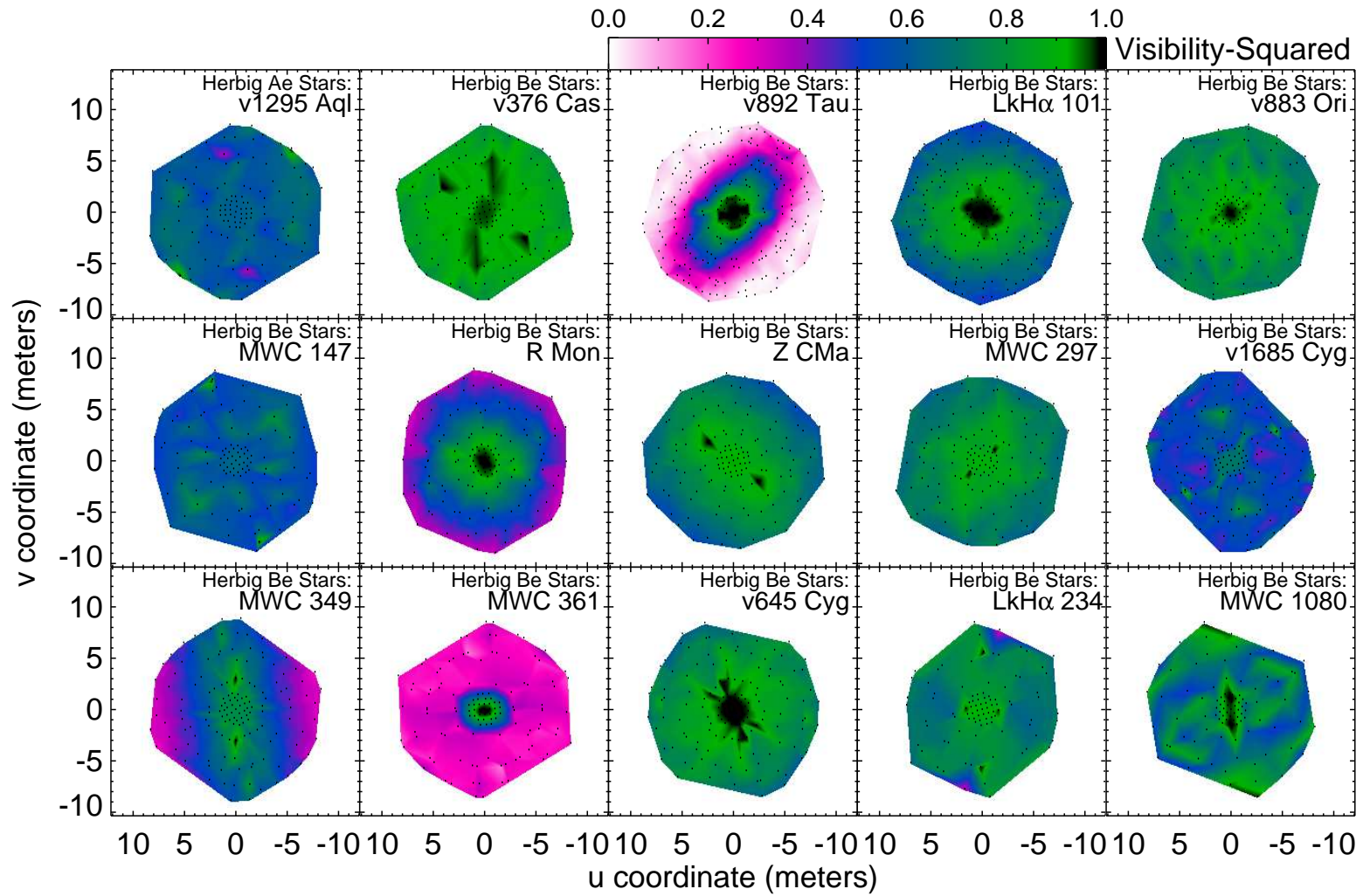


Figure 5 (continued)

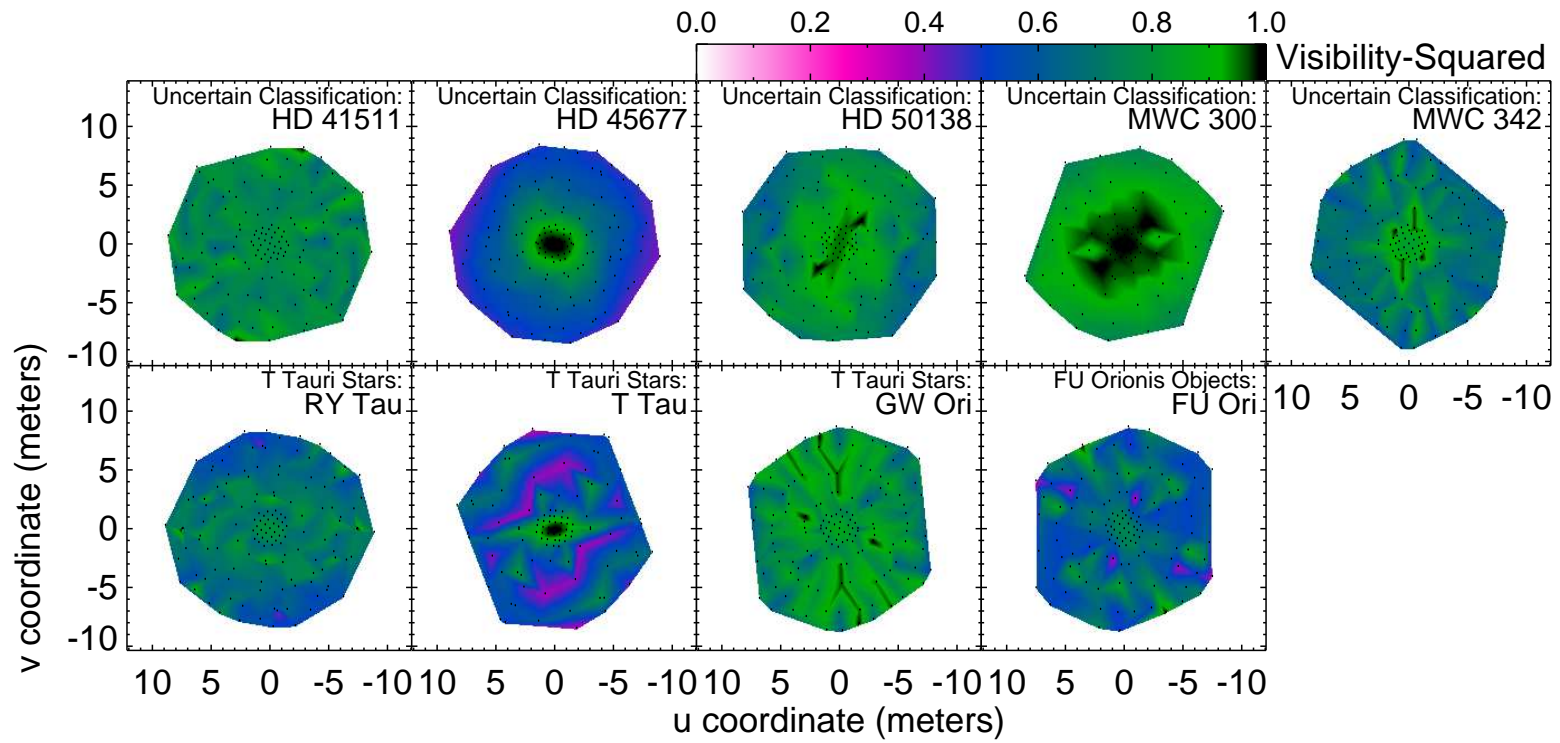


Figure 5 (continued)

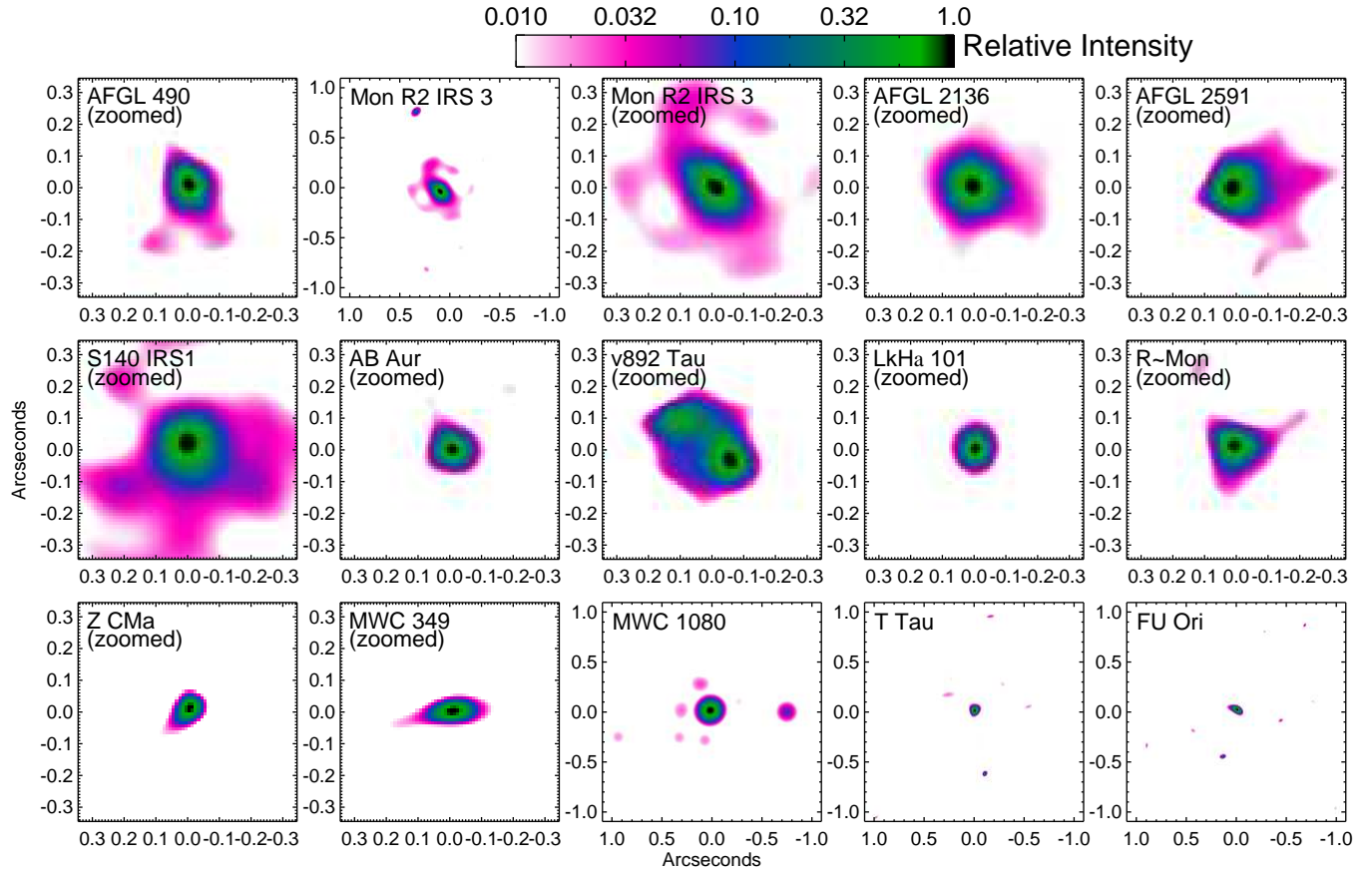


Fig. 6.— This figure shows the aperture synthesis images of the most resolved targets in our sample. The intensity scale is logarithmic and is specified in the color bar. North is up and East is left in all figures.

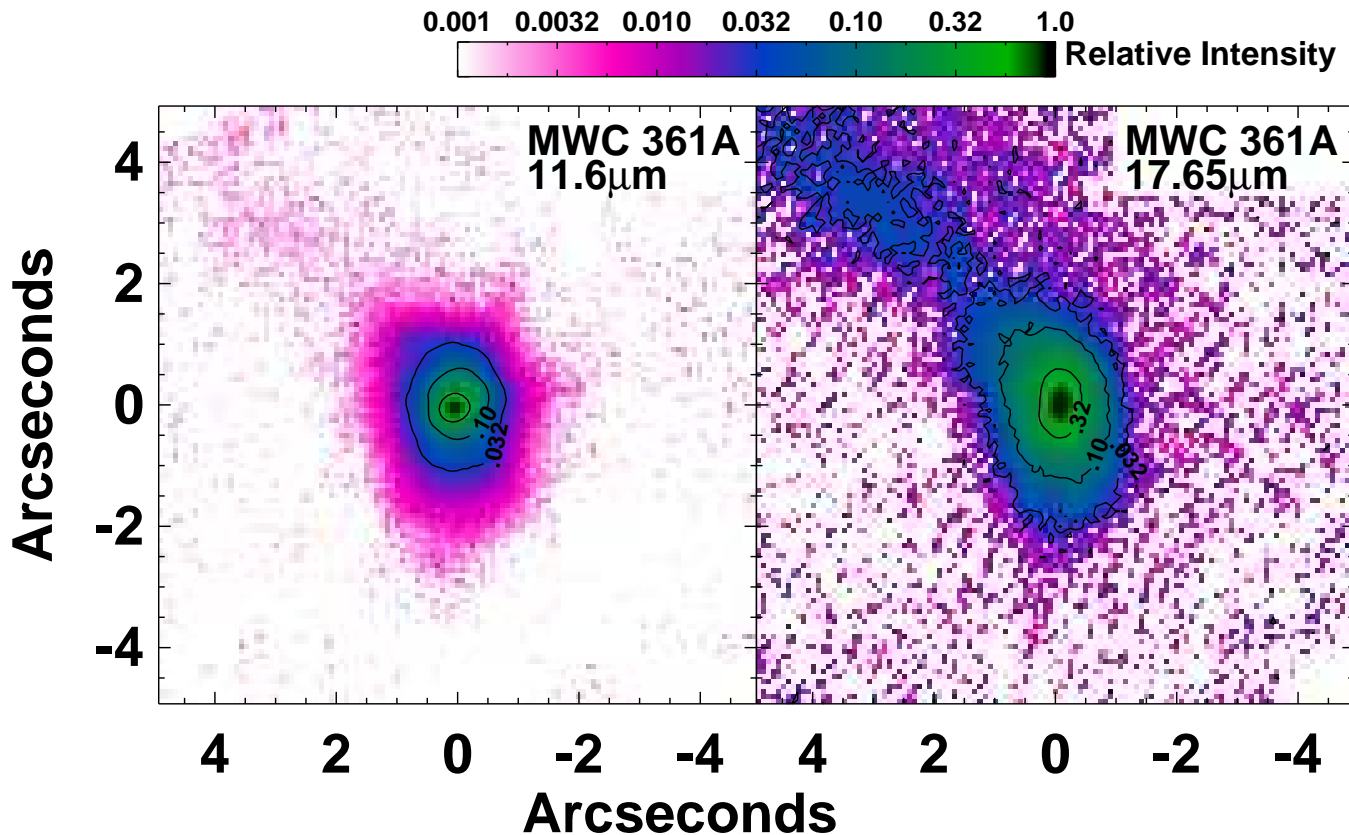


Fig. 7.— This figure shows imaging of MWC 361A at 11.6 μ m and 17.65 μ m using the LWS camera on the Keck telescope without segment-tilting (first presented in Perrin 2006). We see an arcsecond-scale North-South extension which follows the orientation of the underlying sub-arcsecond binary in this system (Monnier et al. 2006). This is a remarkable structure suggesting the circumbinary disk is in an advanced stage of photoevaporation. The intensity scale is logarithmic and is specified in the color bar. North is up and East is left in all figures.

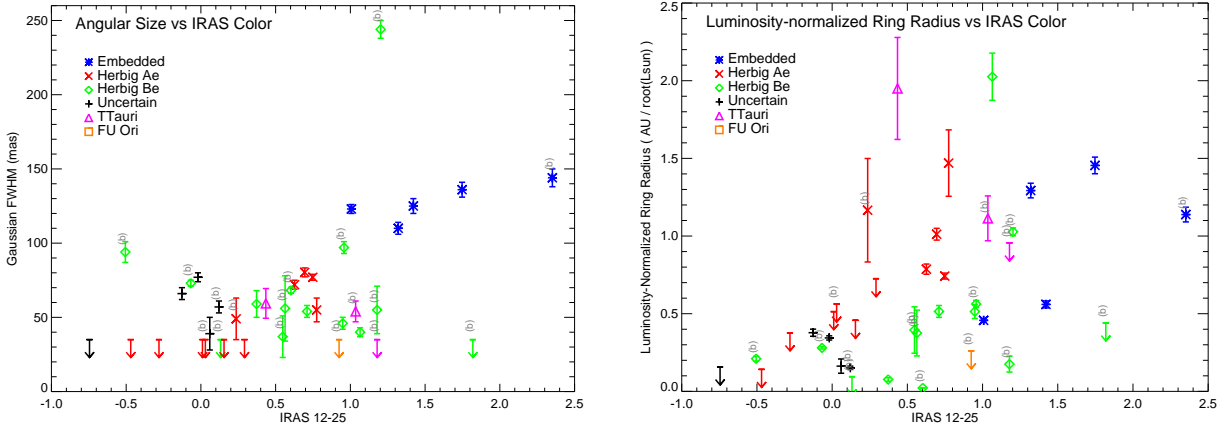


Fig. 9.— (*left panel*) a. The mid-infrared angular size (Gaussian FWHM) vs. IRAS 12-25 color ($-2.5 \log F_{\nu}(12\mu\text{m}) / F_{\nu}(25\mu\text{m})$). Systems in close binaries are labeled (b). Objects with FWHM sizes smaller than 35 mas are shown as 35 mas upper limits. (*right panel*) b. Here we plot the luminosity-normalized ring radius (AU/ $\sqrt{\text{luminosity}}$) as a function of the IRAS 12-25 micron. The luminosity-normalized ring radius is independent of distance and is diagnostic of disk structure. Note the significant correlation for the Herbig Ae sample.